Quantum Phase Characterization via Entanglement Scaling in Fermionic Quantum Wires

Cameron, Alexander Carlo

UNIVERSITY OF CALGARY

Quantum Phase Characterization via Entanglement Scaling in Fermionic Quantum Wires

by

Alexander Carlo Cameron

A THESIS

SUBMITTED TO THE FACULTY OF GRADUATE STUDIES

IN PARTIAL FULFILLMENT OF THE REQUIREMENTS FOR THE

DEGREE OF MASTER OF SCIENCE

GRADUATE PROGRAM IN PHYSICS AND ASTRONOMY

CALGARY, ALBERTA

OCTOBER, 2019

Abstract

Quantum entanglement is studied in the context of its use as a probe of quantum phases within fermionic non-interacting quantum wires. In particular, we consider the uniform lattice, as well as the Su-Schreiffer-Heeger (SSH) model, and use the bipartite entropy of entanglement to characterize their quantum phases. In 1D, it has been shown analytically that the von Neumann entropy defined for a subsystem $\mathcal{H}_A \subset \mathcal{H}_A \otimes \mathcal{H}_B$ takes distinct forms dependent on the whether or not the state is thermodynamically gapped. It is also known that entanglement can be used to identify topological phases of a quantum system, such as the symmetry protected phase found in the SSH model. These results are confirmed numerically, and some common techniques for the calculation of bipartite entanglement are compared according to their aptitude for simulating larger and more complicated systems.

Acknowledgements

Foremost, I would like to express my heartfelt gratitude to Mother Earth for bestowing upon us the abundance that allows us to thrive as a communal species and undertake such creative and curious endeavours. May our intellectual pursuits help us to (re)connect with Her, as we further come to know our selves and neighbours, in harmony.

I would also like to thank the University of Calgary, and the Department of Physics and Astronomy, for their spatial and financial support, which has allowed me to embark on this scholarly quest at all. As well, for the opportunity to participate in the 2017 Summer School on Particles, Strings, and Cosmology, I would like to thank the Universität Hamburg, for their engaging courses and warm hospitality.

To my supervisor, Dr. David Feder, I would like to express my sincere appreciation for the patience and encouragement shown throughout the course of this degree. Thank you for your guidance through the nebulous realm of condensed matter, and your keen eyes on the many revisions of this work. As well, to my committee members Dr. David Hobill, and Dr. Gilad Gour, for their insightful questions and helpful comments.

In addition, to the campus community on large, including all my professors, collaborators, peers, students, friends, and everyone who has cared to share a smile in the hallways and outside. Your compassion and enthusiasm have made a great impact on my life here. And certainly, to my family, for supporting me wholly, I appreciate and love each one of you.

Bless!

Table of Contents

List of Figures and Illustrations

List of Symbols, Abbreviations and Nomenclature

Symbol or abbreviation	Definition
1D	One-Dimensional.
CLM	Correlation Matrix.
DM	Density Matrix.
MBQC	Measurement Based Quantum Computing.
QC	Quantum Computing.
QIP	Quantum Information Processing.
RDb	Reduced Density block.
RDM	Reduced Density Matrix.
SPT	Symmetry Protected Topological.
SSH	Su-Schreiffer-Heeger.
SVD	Singular Value Decomposition.
TEE	Topological Entanglement Entropy.
vN	von Neumann.
$\mathcal{H}$	Hilbert Space.
$\|\emptyset\rangle$	Vacuum state.
$\|\phi\rangle$	Single-body basis mode.
$\|\Phi\rangle$	Many-body basis mode.
$\|\psi\rangle$	Single-body quantum state.
$\|\Psi\rangle$	Many-body quantum state.
$X = \{x_1, \cdots, x_F\}$	Set of occupied sites x_i on the direct lattice.
$\|X\rangle$	Many-body basis mode defined by the set X.
$\|\Phi(X)\|$	Slater determinant defining the ground state amplitude of mode X.
L	Length of a lattice.
F	Population of fermions on a lattice.
ℓ	Length of a contiguous subsystem.
f	Population of a contiguous subsystem.
$\gamma_k(x)$	Mode amplitude for fermion at site x with quantum number k.
$\mathcal{M} = \{\gamma_k(x)\}$	Set of mode amplitudes on a given lattice.

Chapter 1

Introduction

Many novel systems of interest to quantum information processing and other forthcoming inventions exist as exotic *quantum phases of matter*, often classified according to the sorts of order found within given system states [1, 2]. For example, the superconducting phase is characterized by a vanishing electrical resistance, allowing for uninhibited current flow, finding use in a slew of present and future technologies. The studies of materials properties, particularly for systems of the colder and denser varieties, are performed in the name of condensed matter physics; wherein, the quest for room-temperature superconductivity has served as a guiding star for much of the research within the past few decades. Along the way, a wealth of new and intriguing quantum phases have been hypothesized and observed, including superfluids [3], quantum spin liquids [4], and topological insulators [5], for instance. The theoretical explanation and predictions of where and how to find these and other quantum phases is an active area of contemporary research.

In contrast to their classical (thermal) counterparts (eg. liquid, gas), quantum phases and quantum phase transitions occur specifically at ultra-cold temperatures (i.e. absolute zero[1]) where thermal fluctuations are effectively frozen out [1]. Instead, the dominant fluctuations

[1]For the scope of this work, it is sufficient to consider quantum phases as they exist at absolute zero.

are of a quantum nature, deriving from the uncertainty principle, and driven by variations in the physical parameters of the system (e.g. pressure, magnetic field). Both thermal and quantum phases may be thought of as collections of states displaying particular types of order, for example: crystalline order in a solid, or magnetic order in a ferromagnet. Phase transitions are thus identified by the characteristic changes of these orders around *critical points* in the system's phase space [1, 6].

Traditionally, the orders exhibited by the microscopic degrees of freedom within a quantum phase are quantified by some associated *order parameter* that takes finite value in the phase, and vanishes at its boundary [6, 7]. These order parameters are central to the Landau-Ginzburg theory of phase transitions [8, 9, 7], which uses the order parameter(s) tied to a phase transition to effectively describe the system's free energy in the vicinity of its phase boundary. The critical point of phase transition is then determined by the (singular) point in phase space for which this effective free energy takes a non-analytic form. Since the order parameter is often tied to a symmetry exhibited by the phase, phase transitions may also be identified by points of symmetry breaking [1, 6].

While the symmetry-breaking approach to phase boundaries is well suited for many quantum phases, there exist instances of quantum states exhibiting the same symmetries yet distinct physics [10, 11]. Such states are examples of more general *topological quantum phases*, which offer great promise within fault-tolerant quantum computing [12, 13] and which were the subject of the 2016 Nobel Prize in Physics [14, 15, 16]. To extend the traditional paradigm to include topological phases of matter as well, a more fundamental perspective of quantum phases is therefore sought beyond traditional order parameters.

A growing trend in recent years is the use of *entanglement measures* as a fundamental probe of quantum phases, and consequent identification of quantum phase transitions by these means [17, 18, 2]. The presence of quantum entanglement within descriptions of quantum phases should not come as too much of a surprise, as entanglement is fundamentally

a phenomenon of order within quantum systems; a type of correlation beyond the descriptions of classical probability theory, with profound implications on the fundamental nature of reality as we (believe we) know it [19, 20, 21]. Intuitively, we can imagine these non-local correlations as ways of sharing quantum information among the many bodies within a system, and so we might anticipate a connection here to the sorts of order used to define a quantum phase.

A popular choice for a quantitative measure of order within a (quantum) phase is the use of an *order parameter*, often obtained from an $n-$body correlation function measured over the state. The behaviour of the order parameter across the critical point determines the type of phase transition: a discontinuity at the critical point constitutes a first-order transition, while a continuous, yet non-analytic critical point is second-order. First-order phase transitions have the property of coexistence of the two phases on either side of the critical point, while second-order transitions forbid this. In this work, we consider disparate phases within a non-interacting fermionic model, which are separated by a continuous transition.

For continuous (second-order) phase transitions, we know that a phase boundary is characterized by a diverging correlation length in the single-body correlation functions of the system [1, 22]. Within the past decade or so, these correlation functions have been found to imply specific behaviours on measures of entanglement within the system: the von Neumann (vN) entropy, in particular [23, 24, 25]. These findings (among others [26, 27, 28, 29, 30, 17]) support the use of entanglement itself for the detection of quantum phase transitions, and offers the further possibility to enrich our understanding of the fundamental nature of the emergent properties exhibited in these quantum systems.

Instead, topological phases are defined using global order parameters are needed for these phases, reflecting the global nature of the topological properties we are interested in. One universal measure of global order in a quantum system is the *topological entanglement entropy (TEE)* [31]. The TEE can be extracted from the vN entropy by partitioning the system of

interest in many ways and extracting the component of the vN that is insensitive to the local form of the partition, in the thermodynamic limit. The TEE has also been shown to relate to the quantum dimension of the system [32], indicative of the degeneracy of the topological manifold underlying the system.

While analytical results exist for the entanglement used to characterize quantum phases, the results assume the so-called *thermodynamic limit* of infinite system size and fixed particle density [23, 24, 25]. For real systems however, especially those prepared within table-top experiments [33, 34], we know our system will be finite in extent, and thus should ask how well these results apply to systems away from the thermodynamic limit. This thesis serves to review some of the uses of entanglement within condensed matter theory, and confirm the use of the von Neumann entropy in the identification of a simple topological phase in finite systems. This work explores the efficacy of the thermodynamic results with respect to finite-sized calculations, and analyzes three methods for computing entanglement within fermionic systems in terms of applicability and efficiency.

Within this thesis: Chapter 2 is meant to provide mathematical background for the quantum informational tools we will use in this work. Chapter 3 introduces the relevant concepts and models that will serve as the focus of study. In Chapter 4, we apply the tools from Chapter 2 to the models of Chapter 3 and discuss the algorithm(s) developed to study these finite systems, the results of which are presented and discussed in Chapter 5. Finally, Chapter 6 provides a summary and outlook for future study.

Chapter 2

Key Concepts in Quantum Information

The basic ethos of quantum information theory is the interpretation of pure state outcomes of a given quantum system as logical units of information (classical *bits* being the binary unit of information) [35]. In a two-level quantum system, we encode a quantum bit, termed a *qubit*; a three-dimensional system constitutes a *qutrit*, and so on. In general, a $d-$level quantum system is referred to as a *qudit*. Physically, the logical states of the qudit are embodied by the observable states of the $d-$level quantum system, which are known to exist in superposition for a general quantum state (before measurement). In fact, many advantages of quantum algorithms over their classical counterparts stem from their use of the quantum superposition (and entanglement) between these observable states.

For a system in superposition of observable states, performing measurement on the system will 'collapse' the system[1] into any one of the pure states, where the probability of observing a given state is determined by its amplitude in the superposed state. Having encoded information into the observable states of quantum systems, one may perform physical

[1] according to the Copenhagen interpretation.

operations on the host system such that the quantum logical algorithms are developed such that physical actions on the host system will evolve the encoded information. Such a protocol will effectively transmute a logical input (state) algorithmically to its final output (state) to be measured and interpreted logically. A system in which these states are generated and evolved to perform such algorithms therefore earns the term *quantum computer* [36, 35]. The surrounding infrastructure by which quantum systems are used to communicate quantum data is dubbed a *quantum network* [37, 38, 39], and the two concepts are both renowned for their promise of the forthcoming second information-revolution.

2.1 State Descriptions in Quantum Mechanics

Recall that a pure quantum state of some system is elegantly represented by a normalized vector $|\Psi\rangle$ in some appropriate Hilbert space $\mathcal{H}$. A single-body system lives within a single-body Hilbert space, which is canonically isomorphic to the complex space of dimension d

$$\mathcal{H}^{(1)} \cong \mathbb{C}^d, \tag{2.1}$$

where the dimension d reflects the number of orthogonal states that one may measure the system in. In this sense, the basis of orthogonal state vectors $|\phi_j\rangle$ is meant to correspond to the basis in which measurements are taken. For example, a two-level system (such as the spin of an electron) may take the natural basis $\{|\downarrow\rangle,\ |\uparrow\rangle\}$ defined by the spin-orientation relative to the z-axis. Then defining a basis for measurement equivalently fixes the physical interpretation of the standard orthonormal vectors $|j\rangle$ spanning the Hilbert space, where a corresponding probability amplitude $\alpha_j = \langle\phi_j|\psi\rangle$ represents the likelihood of observing our superposed system $|\psi\rangle$ in the jth mode $|\phi_j\rangle$. In general, our one-body system exists in superposition over its possible basis states prior to measurement, represented by a (normalized)

linear combination

$$|\psi\rangle = \sum_{j=1}^{d} \alpha_j |\phi_j\rangle; \quad \sum_{j=1}^{d} |\alpha_j|^2 = 1. \tag{2.2}$$

For systems of N identical and independent bodies, we may construct the appropriate Hilbert space from the tensor product of N copies of the single-body space

$$\mathcal{H}^{(N)} = \bigotimes_{i=1}^{N} \mathcal{H}_i^{(1)}. \tag{2.3}$$

Letting $J = \{j_1, \cdots, j_N\}$, the basis elements $|\Phi_J\rangle$ spanning the joint space $\mathcal{H}^{(N)}$ are constructed by taking tensor products over the collections of constituent basis elements $|\phi_{j_i}\rangle$

$$|\Phi_J\rangle = |\phi_{j_1}\rangle \otimes |\phi_{j_2}\rangle \otimes \cdots |\phi_{j_N}\rangle, \tag{2.4}$$

and the many-body states are linear sums over the many-body basis

$$|\Psi\rangle = \sum_{J} \alpha_J |\Phi_J\rangle. \tag{2.5}$$

For a bipartite Hilbert space $\mathcal{H}_A \otimes \mathcal{H}_B$,

$$|\Psi\rangle = \sum_{a,b} M_{ab} |\Phi_a\rangle \otimes |\Phi_b\rangle \tag{2.6}$$

where the sum is taken over the many-body basis states $|\Phi_a\rangle \in \mathcal{H}_A$ and $|\Phi_b\rangle \in \mathcal{H}_B$, with M_{ab} the amplitude of the joint state, obtained from the appropriate (anti)symmetrization of the constituent amplitudes.[2]

[2]More on (anti)symmetrization and many-body statistics in Section 3.2.

2.1.1 Pure -vs- Mixed States: The Density Matrix

States that can be represented by single vectors $|\Psi\rangle$ in Hilbert space are said to be *pure states*. All other quantum states are said to be *mixed states*, existing as statistical ensembles of pure states in the Hilbert space. To properly describe these mixed states, we introduce the density matrix (DM) [35, 21]

$$\rho = \sum_i p_i |\Psi_i\rangle\langle\Psi_i|, \tag{2.7}$$

where p_i is the probability of finding your system ρ in the pure state $|\Psi_i\rangle$. Since the p_i constitute a probability distribution of pure quantum states, all density matrices are subject to the normalization condition $\mathrm{Tr}(\rho) = \sum_i p_i = 1$. In the special case of a single non-trivial element of the probability distribution $p_1 = 1$, the DM is *pure*, representing the pure state $|\Psi\rangle$. Since $|\Psi\rangle$ is normalized, pure state density matrices satisfy the following trace condition:

$$\mathrm{Tr}(\rho^2) = \mathrm{Tr}(\rho) = 1. \tag{2.8}$$

A *mixed state*, on the other hand, will satisfy

$$\mathrm{Tr}(\rho^2) < 1. \tag{2.9}$$

Similar to the partition function of classical statistical mechanics, the DM encodes information about the probability distribution of the possible measurement outcomes for a given quantum state. As such, it is often used to compute expectation values, by taking

$$\langle A \rangle = \mathrm{Tr}[\rho A]. \tag{2.10}$$

As before, we can view joint systems as the tensor product of their individual matrices.

This follows for pure states from the tensor identity $(A \otimes B)(C \otimes D) = AC \otimes BD$. Thus

$$(|\Psi_1\rangle \otimes |\Psi_2\rangle)\,(\langle\Psi_1| \otimes \langle\Psi_2|) = |\Psi_1\rangle\langle\Psi_1| \otimes |\Psi_2\rangle\langle\Psi_2| = \rho_1 \otimes \rho_2. \tag{2.11}$$

Arbitrary joint systems still come as either pure or mixed, depending on their trace conditions. The distinction between the two will be important when quantifying the amount of entanglement within our systems, but let us first look more closely at what it means for a composite system to be entangled in the first place.

2.1.2 Separable -vs- Entangled States

When a pure state DM ρ acting on a joint Hilbert space $\mathcal{H}_{AB}$ may be factored into a product of pure states acting on the respective Hilbert spaces $\mathcal{H}_A$ and $\mathcal{H}_B$

$$\rho = \rho^A \otimes \rho^B, \tag{2.12}$$

the state is said to be *separable* [21]. A separable pure state is also referred to as a *product state*, for obvious reasons. Product states share no information between the two systems, as each constituent remains perfectly well-defined independent of the presence other, as illustrated in Figure 2.1.

For mixed states, a density matrix is separable if it may be expressed as a convex combination of product states from the respective Hilbert spaces [41, 21, 2]

$$\rho = \sum_i p_i \rho_i^A \otimes \rho_i^B, \tag{2.13}$$

where $\rho_i \geq 0$ and $\sum_i p_i = 1$. For example, the state

$$\rho = \frac{1}{2}(|00\rangle\langle 00| + |11\rangle\langle 11|) \tag{2.14}$$

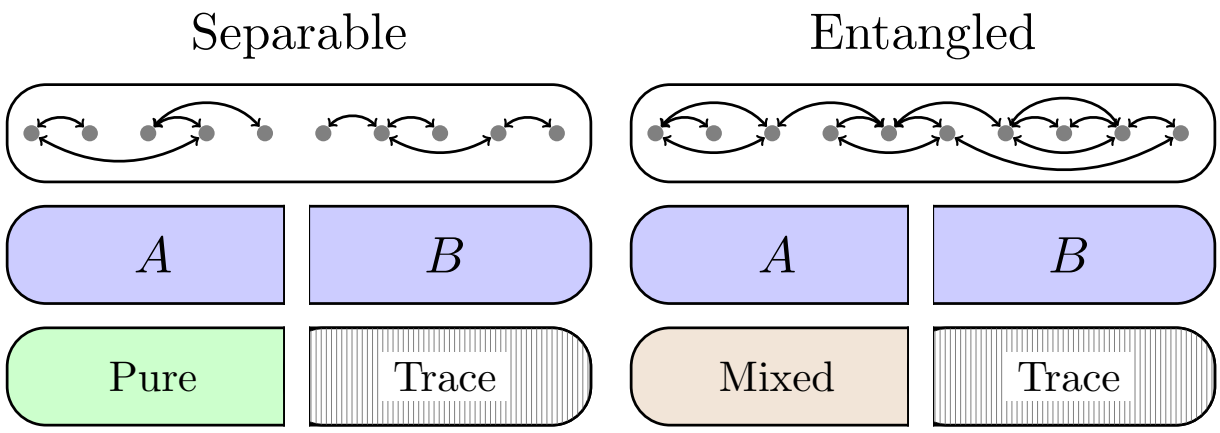

Figure 2.1: A bipartite system is separable when there are no quantum correlations (arrows) between the two sides (A and B) of the system, otherwise, it is entangled. Equivalently, if we are left with a well-defined pure state after tracing out the degrees of system B, then the joint system is separable (left), and entangled otherwise (right). Image inspired by Ref. [40].

may be separated into the following mixture of product states

$$\rho = \frac{1}{2}|0\rangle\langle 0| \otimes |0\rangle\langle 0| + \frac{1}{2}|1\rangle\langle 1| \otimes |1\rangle\langle 1|, \tag{2.15}$$

and is therefore separable. Interpreting the p_i as a statistical distribution of product states, separable states have the property that their correlations may be explained by classical phenomena.

Non-separable states are said to be *entangled*, and their correlations cannot be described by of classical phenomena or local hidden variables [19, 20, 21]. For example, consider the state

$$|\Phi^+\rangle = \frac{1}{\sqrt{2}}\left(|00\rangle + |11\rangle\right). \tag{2.16}$$

Its density matrix is

$$\rho = |\Phi^+\rangle\langle\Phi^+| = \frac{1}{2}\left(|00\rangle\langle 00| + |00\rangle\langle 11| + |11\rangle\langle 00| + |11\rangle\langle 11|\right). \tag{2.17}$$

This state is pure, since $\mathrm{Tr}(\rho^2) = 1$, but we cannot factor it into an ensemble of product states $\rho_i^A \otimes \rho_i^B$, as this would be equivalent to the factoring of Equation 2.16 into well-defined states $|\psi_A\rangle \in \mathcal{H}_A$, $|\psi_B\rangle \in \mathcal{H}_B$, (by the tensor identity used in Equation 2.11). This state is therefore entangled, and in fact, perfectly so, since a measurement of one either of the subsystems in the $\{|0\rangle,\ |1\rangle\}$ basis perfectly specifies the outcome of the other. Physically, this implies the existene of a fundamental connection between the two subsystems, which has found many applications within quantum information processing (QIP) in recent decades [42].

2.1.3 Entanglement as a Resource

Physically, these non-separable states constitute a *resource* for QIP as entangled qubits (or qudits) can be used to encode, secure, and transport quantum information [35, 43]. One instance of QIP particularly relevant to condensed matter systems is the *measurement-based* approach to *quantum computation (MBQC)*, wherein measurement operations on a so-called *resource state* realize quantum logical operations [44]. The measurement based approach to quantum computing has the advantage (over the quantum circuit model, for instance) of adaptation to efficient as well as fault-tolerable instances [44, 45], making it a good candidate for a scalable QIP system. Technologically, our greatest challenge will be to experimentally develop the quantum phases that can host these resource states. For one particular resource, the maximally entangled *cluster state* [46, 47], this has been achieved using ultra-cold atomic gases in optical lattice experiments [44, 48]. The ultra-cold nature of these systems, and other proposals for MBQC using topological states [49] offers a pragmatic motivation for the deeper exploration of quantum informational resources within condensed matter physics.

In addition to strict computation, communication of quantum information through entangled states proves robust against experimental errors [50] and secure against eavesdroppers [37, 38, 39], offering promise of a reliable quantum network for dense information transfer. The design and construction of such an infrastructure depends on the preced-

ing creation of network elements such as quantum relays or quantum repeaters to achieve long-distance teleportation [51, 52, 53] and quantum memories to store quantum information as needed [54, 55, 56]. These memory systems are material by nature, and so knowledge of the informational properties of quantum systems proves immensely valuable to the future of these technologies.

2.2 Measures of Entanglement

Since entanglement is a resource, we should like to know how much of it is present in a given system. Then let us consider a family of functionals $E(\rho)$ that serve to quantify the entanglement within a quantum state ρ. To ensure these functionals measure only quantum correlations, we require they meet the following criteria [57, 58]:

1. $E(\rho) \in \mathbb{R}_0^+$ has real, non-negative valuation.

2. $E(\rho) = 0$ if ρ is separable.

3. $E(\rho)$ does not increase on average under Local Operations and Classical Communication (LOCC)[3], that is to say that if the A_i are Krauss operators [35] describing the transformation, then
$$E(\rho) \geq \sum_i p_i E\left(\frac{A_i \rho A_i^\dagger}{\mathrm{Tr}(A_i \rho A_i^\dagger)}\right), \tag{2.18}$$
where $p_i = \mathrm{Tr}(A_i \rho A_i^\dagger)$ is the probability of finding the ith outcome after the protocol.

4. For a pure state $\rho = |\Psi\rangle\langle\Psi|$, the entanglement measure reduces to the entropy of entanglement[4]
$$E(|\Psi\rangle\langle\Psi|) = S\left(\mathrm{Tr}_B(|\Psi\rangle\langle\Psi|)\right). \tag{2.19}$$

[3]Local Operations include unitary transformations and local measurements.
[4]Refer: Section 2.2.3.

There are a handful of useful functions meeting most, but not all, of the above conditions. A function that satisfies the first three criteria is dubbed an *entanglement monotone*; a function satisfying all four criteria is referred to as an *entanglement measure*. Note that the literature will sometimes relax condition 3 to only those transformations that are deterministic in nature, rather than fully probabilistic [58].

2.2.1 Schmidt Decomposition and the Entanglement Spectrum

One example of an entanglement monotone relevant to our discussion is the *Schmidt Rank*, defined as the number of non-zero *Schmidt coefficients*, which encode the entangled features of a non-separable state. We obtain the Schmidt coefficients through the *Schmidt decomposition* theorem [35].

Theorem 1. (Schmidt Decomposition) *For a pure state $|\Psi\rangle$ in a composite Hilbert space $\mathcal{H}_{AB}$, there exist orthonormal states $|\mathfrak{a}_j\rangle \in \mathcal{H}_A$ and $|\mathfrak{b}_j\rangle \in \mathcal{H}_B$ such that*

$$|\Psi\rangle = \sum_j \sqrt{\lambda_j}|\mathfrak{a}_j\rangle|\mathfrak{b}_j\rangle, \tag{2.20}$$

where the $\sqrt{\lambda_j}$ are real, non-negative scalars satisfying $\sum_j \lambda_j = 1$, known as the Schmidt coefficients.

Proof. Suppose we have a pure state

$$|\Psi\rangle = \sum_{ab} M_{ab}|\Phi_a\rangle|\Phi_b\rangle \tag{2.21}$$

whose coefficients are held in the complex-valued matrix M_{ab}. By the singular value decomposition, we can write $M = UDV^T$ for unitary matrices U, V^T and a non-negative diagonal

matrix D.[5] Then our state takes the form

$$|\Psi\rangle = \sum_{abj} U_{aj} D_{jj} V^T_{jb} |\Phi_a\rangle |\Phi_b\rangle. \tag{2.22}$$

Since U and V are unitaries, we may use them to define a new set of orthonormal bases $|\mathfrak{a}_j\rangle = \sum_a U_{aj}|\Phi_a\rangle$ and $|\mathfrak{b}_j\rangle = \sum_b V^T_{jb}|\Phi_b\rangle$, and relabel $D_{jj} = \sqrt{\lambda_j}$ to obtain

$$|\Psi\rangle = \sum_j \sqrt{\lambda_j} |\mathfrak{a}_j\rangle |\mathfrak{b}_j\rangle. \tag{2.23}$$

Thus, the Schmidt decomposition theorem is a special application of the singular value decomposition, where the Schmidt coefficients $\sqrt{\lambda_i}$ are precisely the singular values of the matrix M_{ab} defining the state $|\Psi\rangle$, as in Equation (2.6). □

Corollary 2. *The number of non-zero Schmidt coefficients defines the* Schmidt rank*, which gives an alternate criterion for entanglement: a state is entangled if and only if its Schmidt rank is greater than one.*

Within the Schmidt decomposition, notice that tracing out either of the two subsystems leaves the same Schmidt coefficients regardless of subsystem choice. Then the set of Schmidt coefficients is especially a good candidate to extract entanglement data from since it is symmetric about the choice of subsystem. In fact, the set $\{\lambda_j\}$ is sometimes referred to as the *entanglement spectrum*,[6] as it is used to compute our measures of entanglement. Further system properties may be derived from this entanglement spectrum as well, studied under the moniker *entanglement spectroscopy* [59, 60].

[5] Note that while matrix D is not square in general, its non-zero elements exist within the square block of size $r \times r$, where r is the (maximum) Schmidt rank of the state.

[6] In recent years, the term *entanglement spectrum* has come to refer to the logarithm of these values, obtained from the so-called *entanglement Hamiltonian* discussed in section 4.1.3.

2.2.2 The Reduced Density Matrix

An alternative method by which to obtain the entanglement spectrum is to compute the *reduced density matrix (RDM)* of the system, by tracing out one of the complementary subsystems

$$\rho^A = \mathrm{Tr}_B(\rho^{AB}) = \sum_b \left(\mathbb{1} \otimes \langle b|\right) \rho^{AB} \left(\mathbb{1} \otimes |b\rangle\right), \tag{2.24}$$

where the partial trace effectively "traces-out" the degrees of freedom of subsystem B to leave a re-weighted mixture of the states of subsystem A. Recalling the Schmidt decomposition $|\Psi\rangle = \sum_i \sqrt{\lambda_i}|\mathfrak{a}_i\rangle|\mathfrak{b}_i\rangle$, we can take the partial trace using the orthonormal Schmidt basis $|\mathfrak{b}_k\rangle$ to see that the eigenvalues of this mixture will be precisely the entanglement spectrum

$$\rho^A = \mathrm{Tr}_B \left(\sum_{ij} \sqrt{\lambda_i \lambda_j} |\mathfrak{a}_i\rangle\langle\mathfrak{a}_j| \otimes |\mathfrak{b}_i\rangle\langle\mathfrak{b}_j| \right) = \sum_i \lambda_i |\mathfrak{a}_i\rangle\langle\mathfrak{a}_i|. \tag{2.25}$$

We see that the RDM of a pure state is therefore mixed whenever the state is entangled, by the Schmidt-rank-criterion above. The statistical ensemble of pure states in this mixture derives from the quantum correlations with the degrees of system in subsystem B that we traced out.

For example, consider the Bell state $|\Phi^+\rangle$. Tracing out one of the subsystems (Bob) leaves the reduced density matrix

$$\rho^A(\Phi^+) = \frac{1}{2}|0\rangle\langle 0| + \frac{1}{2}|1\rangle\langle 1|. \tag{2.26}$$

The Schmidt coefficients are both $\sqrt{\lambda_i} = 1/\sqrt{2}$, and the Schmidt rank is two for this entangled state. The persistent uncertainty in this mixture is tied to the uncertainty associated to a measurement of Bob's state (in the same basis).

2.2.3 Entanglement Entropies

For entanglement within an overall pure state, the entropy of entanglement serves as a good measure [57]. Other measures exist for mixed states as well [61]; however, the entropy of entanglement will suffice for us as we limit our scope to entanglement within pure states. Depending on style, there are a few choices of which entropy to use to measure entanglement; a few choices are discussed below.

von Neumann Entropy

The von Neumann (vN) entropy of a state ρ is defined

$$S(\rho) = -\operatorname{Tr}(\rho \ln \rho), \tag{2.27}$$

in analogue to the Shannon entropy of classical probability [62, 63]. For the sake of computation, it is often easiest to express the vN entropy in terms of the spectrum of ρ. Since we know a density matrix ρ is diagonalizable, the matrix logarithm lets us write

$$\ln \rho = V \ln(P) V^\dagger, \tag{2.28}$$

using the diagonal matrix $P = V^\dagger \rho V$. Making the appropriate substitutions to Equation (2.27), we find

$$S(\rho) = -\operatorname{Tr}\left[V P V^\dagger V \ln(P) V^\dagger\right] = -\operatorname{Tr}\left[P \ln P\right], \tag{2.29}$$

by the cyclic property of the trace. Then since $P = \sum_i p_i |d_i\rangle\langle d_i|$ is diagonal, we have that

$$S(\rho) = -\sum_i p_i \ln p_i \tag{2.30}$$

where the p_i are the eigen-spectrum of the matrix ρ. Notice that this is equivalent to the Shannon entropy, up to choice of base, for the probability distribution $\sum_i p_i = 1$. Interpreting the spectrum of ρ as the probability distribution of the system's outcomes, we see the von Neumann entropy measures the amount of information gained, on average, by a measurement on the system.

When our spectrum is the entanglement spectrum λ_i of the reduced density matrix ρ^A (or ρ^B), the von Neumann entropy serves as a measure of entanglement between subsystems A and B.

$$S(\rho^A) = -\sum_i \lambda_i \ln \lambda_i. \tag{2.31}$$

Notice that the Schmidt decomposition theorem ensures that $S(\rho^A) = S(\rho^B)$ as we would like.

Remark 1. *Recall that the maximally mixed state has maximal entropy classically. We find the same for the entropy of entanglement, and may use this fact to rescale our logarithm. Let us refine*

$$S(\rho^A) = -\operatorname{Tr}(\rho \log_d \rho), \tag{2.32}$$

where d is the dimension of our single-body Hilbert space. Then for a maximally entangled system,

$$\rho^A = \frac{1}{d}(|0\rangle\langle 0| + \cdots + |d-1\rangle\langle d-1|) \implies S(\rho^A) = \frac{d}{d}\log_d(d) = 1. \tag{2.33}$$

Rényi Entanglement Entropies

In classical information theory, the class of *Rényi entropies*,

$$S_\alpha(X) = \frac{1}{1-\alpha} \ln \left(\sum_{i=1}^{n} p_i^\alpha \right), \tag{2.34}$$

are parametrized by an order $\alpha \geq 0,\ \alpha \neq 1$, and defined over a classical probability distribution $X = \{p_1, \cdots, p_n\}$. The Rényi entropies serve to generalize the Hartley entropy, Shannon entropy, and collisional entropy, where these measures are recovered in the cases $\alpha \to 0,\ 1,\ 2$, respectively.

The class of *Rényi entropies* [64, 65]

$$S_\alpha(\rho) = \frac{1}{1-\alpha} \ln \mathrm{Tr}[\rho^\alpha] = \frac{1}{1-\alpha} \ln \left(\sum_\lambda \lambda^\alpha \right), \tag{2.35}$$

parametrized by $\alpha \geq 0$, serve to generalize the von Neumann entropy; where the vN entropy is recovered in the limit $\alpha \to 1$. Physically, the Rényi entropies have been interpretted as related to the derivatives of the free energy of a system in thermal equilibrium [66], are useful for fractal systems [67], and have been interpreted in gravitational contexts as well [68]. Mathematically, the Rényi entropies are useful for further characterizing quantum channels in terms of mutual information [69], and for constructing proofs [70, 71] . In terms of condensed matter, the Rényi entropies and derived mutual information have been found to follow similar scaling laws as the vN entropy, however, they will not be the main focus of this work.

2.2.4 Area Laws for Entanglement

The entanglement entropies (and vN entropy in particular) have found themselves the focus of many studies investigating the scaling behaviour of these quantities in the size of the subsystem [18]. Within these studies, a rather intriguing result is found: contrary to the entropy of thermal systems, which scales with the volume of the systems, the entanglement of many ground states is found to scale with the area of the surface ∂A defining the partition A, as in Figure 2.2

$$S(A) \sim \partial A. \tag{2.36}$$

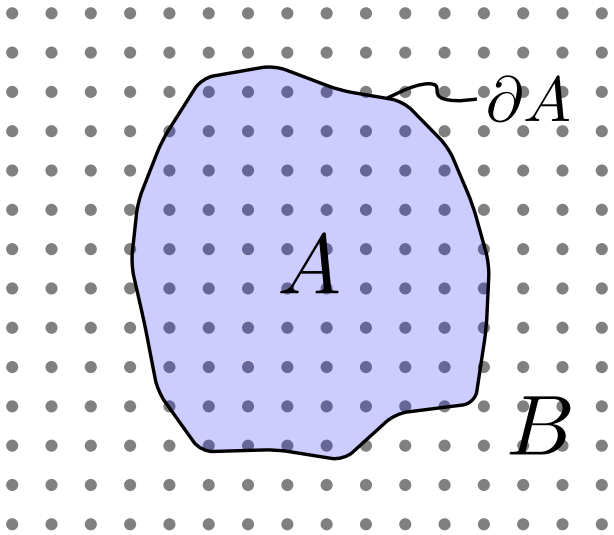

Figure 2.2: The area law states that the entanglement entropy between two contiguous regions A and B within a fixed system will scale with the size of the minimal surface bounding ∂A the region A.

This so-called *area law* is especially curious in the context of quantum gravity for its striking resemblance to the Bekenstein-Hawking entropy of a black hole [72, 73, 74], prompting many speculations into the quantum nature of these objects [75, 76, 77]. In particular, there is much ado lately surrounding the theory of *emergent gravity* within the context of holography and the AdS/CFT correspondence [78, 79, 80], suggesting that our understanding of modern gravitation happens to be a dual description of entangled quantum systems in fewer dimensions. For systems in one dimension (1D), any contiguous partition will be defined only by its two end-points, regardless of its size. A 1D area law then manifests as a saturation of the entanglement to some constant value, independent of the size of the partition.

Within condensed matter, the area law is often a tool used to characterize quantum phases and identify quantum phase transitions, marked by correction factors and sub-leading terms. The general intuition is that an area law will appear for phases with short-ranged

correlations, and this has been proven in 1D [23]. Examples of area law scaling exist for higher-dimensional systems as well [81, 82], but a general proof has not yet been completed for these larger systems. Part of the motivation for numerical calculations of the entanglement entropy is to continue to build intuition for these higher-dimensional systems, as well as to extend the entanglement characterization to more physical Hamiltonians, such as interacting models, which can not be solved analytically.

Quantum critical states, such as free-fermions [25, 18], and some other gapless states can be characterized by long-ranged correlations that lead to violations of the area law is subject to corrections, often logarithmic in the length of the subsystem [83, 84]

$$S(A) \sim \log(\ell_A)\partial A. \tag{2.37}$$

As gapless (critical) states mark the boundary between two gapped phases of matter, the appearance of a logarithmic correction to the area law may be used to signal a quantum phase transition.

In the case of a topologically ordered state, the long-ranged correlations are found to be concentrated in an additive term γ, dubbed the *topological entanglement entropy* (TEE) [31]

$$S(A) \sim \partial A - \gamma. \tag{2.38}$$

From the TEE may be extracted information about the topology underlying the state, and thus the TEE may be used to differentiate different topological phases sharing otherwise similar features [2].

Chapter 3

Quantum Phases and Lattice Systems

Many solid-state and condensed matter systems are conveniently modelled by a lattice geometry. The discrete nature of a lattice proves good representation of the atomic structure of crystalline systems, lending its hand to the recovery of electronic properties from the many-body dynamics of valence electrons, for instance [85]. For quantum lattice systems, discrete Hamiltonians are frequently used to describe the physics of the system in terms of energetic contributions from various mechanisms at play in the model. In this chapter, we cover some brief theory of quantum phases and then consider a simple Hamiltonian applied to two types of lattice, deriving the forms of the eigenstates and dispersion relation for both.

3.1 Quantum Phases of Matter

The different forms of order that persist in a quantum system near absolute zero define the allowed *quantum phases* of the model. These quantum phases are in analogy to classical phases of matter (eg. solid, gas), which also exhibit order, but are mainly driven by thermal fluctuations [1]. Common examples of quantum phase transitions are the transition from a Mott insulating phase to a superfluid, driven by the on-site interaction strength [86], or

the transition to the Quantum Hall state in a two-dimensional electron gas, driven by an external magnetic field [87].

Knowing the physical properties of these phases, we can characterize and identify them using single- and many-body correlation functions, to probe the occupations of relevant modes within the system. For example, the form of the single-body correlation function $g^{(1)}(x) = \langle n_k \rangle$ can be used to distinguish between the Mott insulating, and superfluid phases of the Bose-Hubbard model, by considering the occupation density of the lowest energy mode k_0 compared to the rest of the allowed levels. Similarly, the spatial correlation function $C(x) = \langle c_0^\dagger c_x \rangle$ considers the range of correlations in a given state, and can be used to distinguish quantum phases as well.

Depending on the spatial distribution of the single-body correlation function, it can be well-approximated by either an exponential function

$$C^{(1)}(x) \sim e^{-|x|/\xi}, \tag{3.1}$$

with a finite correlation length ξ; or algebraically as a power-law

$$C^{(1)}(x) \sim |x|^{-\alpha}, \tag{3.2}$$

implying a divergent correlation length and long-ranged correlations. It was shown in [24] that a finite correlation length implies a thermodynamically gapped state in a 1D system. This result is in confirmation of an apparent intuition, that a gapped system should exhibit more localized phenomena in the ground state, compared to a gapless (or critical) state, for which correlations are known to be long-ranged, exhibiting power-law scaling across many systems at different length scales throughout complexity science.[1] In addition, Hastings'

[1] From neurons in the brain, to the crystallization of water, to wildfires, these critical systems all seem to obey power-law scaling [88].

result was extended to say that a finite correlation length implies an entanglement area law within one-dimensional systems [23], further cementing the connection between quantum phase characteristics and quantum entanglement. Intuitively, this result predicts a saturation in the entanglement entropy as the size of the subsystem grows, since the correlations are localized to the zero-dimensional boundary points defining the subsystem. For higher-dimensional systems, the area law has been demonstrated in a number of gapped systems [81, 82], although the rigorous proof of whether this is always the case or not remains an open problem. Extending the theory to include entanglement in higher dimensions will help elucidate the role locality plays in the forms of order defining quantum phases, and should assist our understanding of quantum matter at large.

3.1.1 Topological Phases of Matter

Beyond merely the presence or absence of a thermodynamic gap, quantum phases, and specifically, second order phase transitions, are often characterized by an appropriately defined *order parameter*, tied to a local symmetry in the Hamiltonian that is broken at the phase boundary [2, 7]. For example, net magnetization serves as the order parameter for the ferromagnetic state, which vanishes at its phase boundary. However, not all types of quantum phases can be modelled in this manner.

One particularly interesting class of quantum matter is topological quantum matter. Define a *topological phase* as one whose properties are invariant under diffeomorphisms (smooth transformations) in phase space [2, 13]. This invariance precludes the effectiveness of local order parameters, as the local neighbourhoods on which they may be defined might vary in the diffeomorphism. For these phases, topological invariants and order parameters of a global nature are thus required.

In the language of quantum information, the entanglement spectrum and the topological entanglement entropy are used to characterize the topological properties of matter of im-

mense technological interest [89, 90, 91]. Topological phases are known to host exotic quasi-particles obeying fractional (anyon) statistics, well-suited for quantum computing (QC) [13]. Developing a theoretical framework to identify and describe these states will not only assist their experimental realization, but an informational-theoretic framework for these phases may offer an advantage creating topological quantum algorithms as well.

3.2 Many Body Quantum Systems

When thinking of pure states of many-body quantum systems, it is most natural to use the second-quantized formalism, in which observable states are identified by the sets of occupation numbers n_j associated to each distinguishable mode $|\varphi_j\rangle$ in the system. In the second-quantized formalism, Hilbert spaces of many identical bodies are spanned by sets of *Fock states* [92]

$$|n_1, \cdots, n_d\rangle \in \mathcal{H}^{\otimes N}, \tag{3.3}$$

where $\mathcal{H}^{\otimes N}$ is the N-body joint space built from $N = \sum_{j=1}^{d} n_j$ copies of the d-dimensional, single-body space $\mathcal{H}$. The second-quantized creation $a_j^\dagger$ and annihilation a_j operators act on these Fock states as maps between spaces of adjacent particle numbers[2]

$$\begin{aligned} a_j^\dagger :\ & \mathcal{H}^{\otimes N} \to \mathcal{H}^{\otimes (N+1)}; \\ & |n_j\rangle \mapsto \sqrt{n_j + 1}|n_j + 1\rangle \end{aligned} \tag{3.4}$$

$$\begin{aligned} a_j :\ & \mathcal{H}^{\otimes N} \to \mathcal{H}^{\otimes (N-1)}, \\ & |n_j\rangle \mapsto \sqrt{n_j}|n_j - 1\rangle \end{aligned} \tag{3.5}$$

[2]Note that these operators affect only the specified mode j, so the rest of the modes have been omitted from these definitions. Note also that if $a^\dagger$ is a fermionic operator, then Pauli exclusion forces $n_j \in \{0, 1\}$ for all modes in the system.

analogous to the ladder operators between excited states of the quantum harmonic oscillator. The Fock state devoid of any particles is the vacuum state $|\emptyset\rangle := |0, \cdots, 0\rangle \in \mathbb{C}$. Since these operators explicitly vary the dimension of our Hilbert spaces, each of these $N-$body Hilbert spaces must be embedded simultaneously into some larger space so that our operators are defined globally on the Fock space. *Fock space* is thus constructed as the direct sum of n-body Hilbert spaces

$$\mathcal{F} = \bigoplus_{n=0}^{\mathfrak{N}} \mathcal{H}^{\otimes n}, \tag{3.6}$$

ranging n from zero to some sufficiently large $\mathfrak{N}$, as needed. In the general quantum field theory, Fock space is often taken to be infinite dimensional, although a finite-dimensional space suffices for a finite system. Such is the case for the models considered here.

Using the second-quantized formalism, the many-body basis states $|\Phi\rangle$ of a fixed Hilbert space $\mathcal{H}^{\otimes N}$ are given by strings of creation operators acting on the vacuum state $|\emptyset\rangle \in \mathcal{H}^{\otimes 0}$

$$|\Phi_I\rangle = \left(\prod_{i\in I} a_i^\dagger\right)|\emptyset\rangle, \tag{3.7}$$

for an appropriate index set I. A general pure state may then be formed from a superposition of these basis states

$$|\Psi\rangle = \sum_I \Gamma_I \left(\prod_{i\in I} a_i^\dagger\right)|\emptyset\rangle, \tag{3.8}$$

where Γ_I is the state amplitude for the basis state $|\Phi_I\rangle$ in the superposition.

3.2.1 Particle Statistics

Recall there are two types of quantum particle: fermions and bosons. Each type obeys its own set of statistics which can be specified in the second-quantized formalism by a corresponding algebra.

Bosons

Bosonic particles are those that are symmetric under particle exchange. Assuming we can distinguish between the bosons, say one is red and one is blue, then the first quantized wavefunction looks like

$$\psi_r(x_1)\psi_b(x_2) = \psi_b(x_1)\psi_r(x_2). \tag{3.9}$$

In the second-quantized formalism, this condition is reflected in the operator algebra. The bosonic algebra employs the commutator bracket $[A, B] = AB - BA$

$$[b_i^*, b_j^*] = 0; \quad [b_i, b_j^\dagger] = \delta_{ij}, \tag{3.10}$$

where the superscript * denotes the creation ($b^\dagger$), or annihilation (b) operator, as warranted. A two-boson state in this formalism then satisfies

$$b_2^\dagger b_1^\dagger|\emptyset\rangle = b_1^\dagger b_2^\dagger|\emptyset\rangle. \tag{3.11}$$

Bosonic systems are very interesting for their role in Bose-Einstein condensation [1], as Goldstone modes for spontaneous symmetry breaking [93, 94, 95, 96], and as Cooper pairs in the Bardeen-Cooper-Schrieffer (BCS) theory of superconductivity [97]; however, the focus of this thesis is fermionic systems, and so bosons will not be discussed much further.

Fermions

Fermionic states are characterized by their antisymmetry under particle exchange

$$\psi_r(x_1)\psi_b(x_2) = -\psi_b(x_1)\psi_r(x_2). \tag{3.12}$$

In terms of second-quantized operators, the antisymmetry is captured by the fermionic algebra

$$\{c_i^*, c_j^*\} = 0; \quad \{c_i, c_j^\dagger\} = \delta_{ij}, \tag{3.13}$$

where $\{A, B\} = AB + BA$ is the anticommutator bracket and the superscript * serves to indicate either the creation ($c^\dagger$) or annihilation (c) operator, as needed. So that a two-fermion state in this formalism satisfies

$$c_2^\dagger c_1^\dagger |\emptyset\rangle = -c_1^\dagger c_2^\dagger |\emptyset\rangle. \tag{3.14}$$

An important consequence of the fermionic algebra is the Pauli exclusion principle.

Theorem 3. *(Pauli Exclusion) No two fermions can occupy the same quantum state.*

Its proof is remarkably simple.

Proof. Consider the two-body state

$$|\Psi\rangle = \gamma_i c_i^\dagger c_i^\dagger |\emptyset\rangle. \tag{3.15}$$

By the fermionic algebra, we should be able to swap the order of the operators at the cost of a negative sign

$$|\Psi\rangle = \gamma_i c_i^\dagger c_i^\dagger |\emptyset\rangle = -\gamma_i c_i^\dagger c_i^\dagger |\emptyset\rangle, \tag{3.16}$$

and so $\gamma_i = 0$. □

3.2.2 (Spontaneous) Entanglement within Fermionic Systems

Fermionic systems are a natural candidate for study within condensed matter, and especially solid state physics, as the dynamic particles in many physical systems are the valence electrons of the material. An intriguing consequence of the fermionic algebra is the peculiar fact

that a pure fermionic ground state possesses natural entanglement.[3] For instance, consider a system of two modes at equal energies occupied by a single fermion (or boson, in fact). Its ground state is the even superposition of these two modes

$$|\psi\rangle = \frac{|0,1\rangle + |1,0\rangle}{\sqrt{2}}, \tag{3.17}$$

which looks superficially like the $|\Psi^+\rangle$ Bell state. Checking our separability condition, we can see that this state is indeed entangled, although with only a single particle in our system, we might ask the question, "what exactly is being entangled?" To answer, we might first notice that our state in Equation (3.17) is conveniently written in bipartite form $|\psi\rangle = 1/\sqrt{2}|0\rangle|1\rangle + 1/\sqrt{2}|1\rangle|0\rangle$, allowing us to easily read out its Schmidt values: $\lambda_i = 1/2$, giving us one unit of entanglement entropy just as with the Bell states. Then, since our partitioning into the distinguishable modes reveals maximal entanglement, we must conclude that our information has been encoded into the occupations of these modes. The entanglement then persists between these state occupations, stemming from particle conservation, so that the presence or absence of a particle on one mode may be entangled with that of another. In fact, this is the basis for the idea of fermionic quantum computing.

Fermionic Quantum Computing

Appealing to the spontaneous entanglement within fermionic systems, attempts are being made to harness this natural resource for the purposes of QIP. Using fermionic statistics for QC was first proposed in [99], and has been explored as a possibility for MBQC as well [100, 101]. The fermionic approach promises an accessible route to QC through the use of cold-atom experiments in optical lattices [48], and further promise of advanced knowledge of quantum chemistry. Note that a converse implication of [99] is the use of quantum

[3] What is especially peculiar about this fact, from a fundamentals perspective, is that the fermionic ground states often contain more entanglement than their bosonic counterparts [25, 98].

algorithms to model electronic structure within molecules [102, 103].

The trick with coaxing fermions into performing non-trivial quantum computations is to have their systems break classical simulatability. Unfortunately, this is not the case for non-interacting fermionic systems [104], and extensions such as interactions are required to bridge the gap [99, 105].

3.3 The Tight Binding Model

The tight binding model is often used to study the physics of infinite, non-interacting, and homogenous systems, whose electronic behaviour is well approximated by their band structure, most heavily influenced by the underlying lattice geometry [106, 85]. It is often also referred to as the *linear combination of atomic orbitals (LCAO)*, as its Hamiltonian contains only a kinetic term for single-body motion between (atomic) lattice points. Additional terms can be added to account for other physical processes such as interactions and external magnetic fields, at the expense of the application of band structure theory. While these extended models naturally allow for more interesting physics, they come at the expense of simple diagonalization of the model, and are therefore left to extended study for now.

Consider a gas of non-interacting fermions on a (hyper-)cubic lattice, as is studied by Wolf in [25]. This is the so-called tight binding model [106], whose Hamiltonian is

$$H = \sum_{\langle i,j\rangle \in \mathbb{Z}^d} T_{ij} q_i^\dagger q_j, \tag{3.18}$$

where T_{ij} is the hopping strength between nearest-neighbouring sites $\langle i, j\rangle$ on a d-dimensional lattice $\mathbb{Z}^d$. The hopping strength is derived entirely from the geometry of the lattice, as it reflects the degree of overlap between the wavefunctions localized at sites i and j. For a physical picture, consider the movement of free electrons in a crystal (Figure 3.1). The loca-

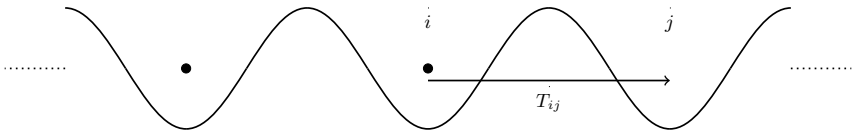

Figure 3.1: The (one-dimensional) tight binding model describes the transport of non-interacting electrons within a system with a periodically varying potential such as a crystal. Let the wells represent the atomic potentials of the nuclei in the crystal. The valence electrons (circles) may hop from one atom i to another j at the cost T_{ij}.

tions of the constituent atoms comprise the lattice structure, to which the valence electrons are bound, though allowed to hop to a neighbouring atom at energy cost T_{ij}. Whereas Wolf studied these free fermions on a lattice of arbitrary dimension, we restrict our focus to exact computation in 1D to start.

3.3.1 A Gapless System: The Bravais Chain

We say that a lattice is *regular*, or *Bravais*, when it looks the same at all points on the lattice [85]. In 1D, there is only one style of Bravais lattice, while higher dimensions allow for more. The 1D Bravais lattice is defined by $T_{ij} = -t$ for all neighbouring sites i, j

$$H = -t \sum_{\langle i,j \rangle} q_i^\dagger q_j. \tag{3.19}$$

This corresponds to an equal spacing of identical atoms in the physical picture.

Eigenstates on the Bravais Chain

The eigenstates of this model correspond to the basis operators for which the Hamiltonian is diagonal

$$H = \sum_k \epsilon_k \phi_k^\dagger \phi_k, \tag{3.20}$$

where ϵ_k is the energy of the state $|\phi_k\rangle = \phi_k^\dagger|\emptyset\rangle$. To find this basis, we will need to fix the boundary conditions of our lattice. There are two main styles of bounds to consider, namely: periodic (Born-von Karman), and terminal bounds, illustrated in Figure 3.2. A periodic

Figure 3.2: Bravais lattices of periodic (Born-von Karman) bounds (left), and terminal bounds (right). The lines between nodes indicate the hopping terms in the Hamiltonian. For the uniform chain, all edges of the graph have the same amplitude and are thus unmarked.

lattice is often used to model physics within the bulk of a crystal, where the boundary effects are negligible. This also applies to the modelling of an infinite lattice in the thermodynamic limit, and so we will focus on these boundaries for this study. The Hamiltonian for a periodic Bravais lattice of length L is diagonalized via the discrete Fourier transform

$$H = \sum_k \epsilon_k p_k^\dagger p_k; \quad p_k^\dagger = \frac{1}{\sqrt{L}} \sum_{x=1}^{L} e^{-ikx} q_x^\dagger, \tag{3.21}$$

where $k = \pm 2\pi m/L;\ m \in \mathbb{Z}$ is called the *crystal momentum*, in anology to the momentum of a free wave. The set of crystal momenta constitute the *reciprocal lattice*, whose sites correspond to the allowed momentum states in the system. To preserve the dimensionality of our Hilbert space, we index these crystal momenta using half-odd-integers in the range, $m \in [-L/2, L/2)$, such that $k \in [-\pi/a, \pi/a]$, where a is the lattice spacing. This interval is called the *first Brillouin zone (FBZ)*, and plays the role of the unit cell of the reciprocal lattice [1]. It is straightforward to verify that these momentum states diagonalize our Hamiltonian,

$$H|\phi_k\rangle = \epsilon_k|\phi_k\rangle; \tag{3.22}$$

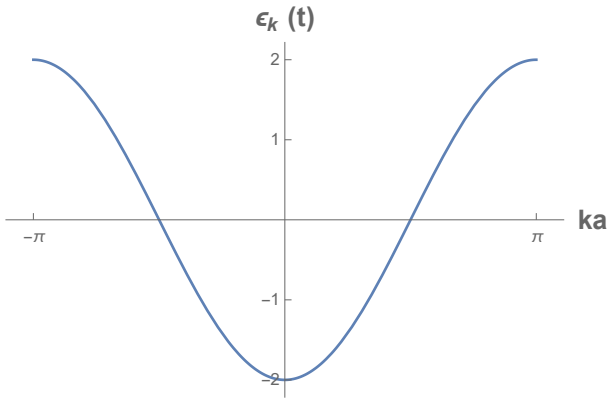

Figure 3.3: Dispersion relation of the tight binding model on the Bravais chain. Notice the lack of a gap between energies in the limit of a continuous reciprocal lattice where $t = 1$ and $a = 1$.

where the energies are

$$\epsilon_k = -2t\cos(ka). \tag{3.23}$$

From our eigenstates then, we may construct pure states at fixed particle number quite simply. A chain with F fermions on an L-site lattice has a ground state defined in the Fourier basis as such:

$$|\Psi_G\rangle^{F,L} = \prod_{k<k_F} p_k^\dagger |\emptyset\rangle \tag{3.24}$$

where k_F is the Fermi level. The general state amplitudes for a fermion on the 1D Bravais lattice are then

$$\gamma_k(x) = \frac{1}{\sqrt{L}} e^{-ikx}. \tag{3.25}$$

Band Structure of the Bravais Chain

The plot of Equation (3.23) shows us the dispersion relation of the Bravais chain. In Figure 3.3 we see that the dispersion is continuous for continuous crystal momenta, therefore, this system is said to be *gapless* for all lattice fillings. Theory predicts that tight binding states of this gapless system should violate the area law logarithmically [25].

3.3.2 A Gapped System: The Dimerized Lattice

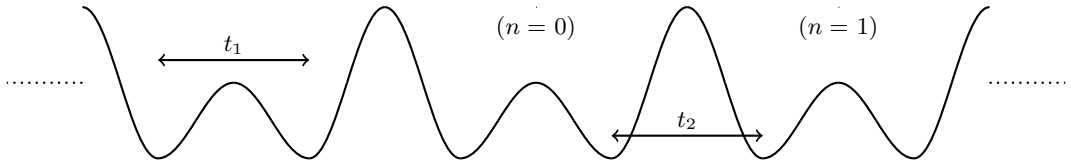

Figure 3.4: The geometry of the SSH model is that of a double-welled lattice with alternating hopping strengths, t_1, t_2 between sites within the same cell (n) and between them, respectively.

Consider a lattice with alternating coupling strengths: $T_{2j,2j+1} = t_1$, $T_{2j+1,2j+2} = t_2$ as depicted in Figure 3.4. Such a lattice is known to many as the Su-Schrieffer-Heeger (SSH) model for polyacetylene [107]. In one dimension and without interactions, the SSH model is described by the Hamiltonian [108]

$$H = -\sum_{j=1}^{L} \left(t_j c_j^\dagger c_{j+1} + h.c. \right); \quad t_j = t[1 - (-1)^j \delta], \tag{3.26}$$

for some energy scale t, and dimerization parameter δ, where $L = 2aN$ is the total length of the lattice, coarse-grained into N unit cells $q_n^\dagger = (c_{n,A}^\dagger \; c_{n,B}^\dagger)$ of two sites. In matrix form, this is

$$H = -\begin{pmatrix} q_1^\dagger & q_2^\dagger & \cdots & q_N^\dagger \end{pmatrix} \begin{pmatrix} U & T & 0 & \cdots & T^\dagger \\ T^\dagger & U & T & \cdots & 0 \\ 0 & T^\dagger & U & \cdots & 0 \\ \vdots & \vdots & \vdots & \ddots & \vdots \\ T & 0 & 0 & \cdots & U \end{pmatrix} \begin{pmatrix} q_1 \\ q_2 \\ \vdots \\ q_N \end{pmatrix}; \quad U = \begin{pmatrix} 0 & t_1 \\ t_1 & 0 \end{pmatrix}, \quad T = \begin{pmatrix} 0 & 0 \\ t_2 & 0 \end{pmatrix}, \tag{3.27}$$

for the intra-cell hopping $t_1 = 1 + \delta$, and inter-cell hopping $t_2 = 1 - \delta$. Our lattice is Bravais over the unit cell $q_n^\dagger = (c_{n,B}^\dagger \; c_{n,B}^\dagger)$, whose length is twice the lattice spacing: $d = 2a$ (d for

dimer). Bloch's theorem then ensures wavelike solutions over these unit cells such that two modes separated by s unit cells differ by a phase: $q^\dagger_{n+s} = e^{-ik(sd)}q^\dagger_n$, prompting the change of basis

$$\begin{pmatrix} q_1 \\ q_2 \\ \vdots \\ q_N \end{pmatrix} = \frac{1}{\sqrt{N}} \begin{pmatrix} \omega & \omega^2 & \omega^3 & \cdots & 1 \\ \omega^2 & \omega^4 & \omega^6 & \cdots & 1 \\ \omega^3 & \omega^6 & \omega^9 & \cdots & 1 \\ \vdots & \vdots & \vdots & \ddots & \vdots \\ 1 & 1 & 1 & \cdots & 1 \end{pmatrix} \begin{pmatrix} p_1 \\ p_2 \\ \vdots \\ p_N \end{pmatrix}, \tag{3.28}$$

where $\omega = e^{2\pi i/N}$ is the N-th principal root of unity. Then our Hamiltonian

$$H = -\begin{pmatrix} q_1^\dagger & q_2^\dagger & \cdots & q_N^\dagger \end{pmatrix} \begin{pmatrix} U & T & 0 & \cdots & T^\dagger \\ T^\dagger & U & T & \cdots & 0 \\ 0 & T^\dagger & U & \cdots & 0 \\ \vdots & \vdots & \vdots & \ddots & \vdots \\ T & 0 & 0 & \cdots & U \end{pmatrix} \begin{pmatrix} q_1 \\ q_2 \\ \vdots \\ q_N \end{pmatrix} \tag{3.29}$$

assumes the block-diagonal form

$$H = -\begin{pmatrix} p_1^\dagger & p_2^\dagger & \cdots & p_N^\dagger \end{pmatrix} \begin{pmatrix} T^\dagger e^{-ikd} + U + Te^{ikd} & 0 \\ 0 & \ddots \end{pmatrix} \begin{pmatrix} p_1 \\ p_2 \\ \vdots \\ p_N \end{pmatrix} = -\bigoplus_{k=1}^{N} \begin{pmatrix} p_k^\dagger \end{pmatrix} H(k) \begin{pmatrix} p_k \end{pmatrix} \tag{3.30}$$

where each block

$$H(k) = \begin{pmatrix} 0 & t_1 + t_2 e^{i2ka} \\ t_1 + t_2 e^{-i2ka} & 0 \end{pmatrix} \tag{3.31}$$

is diagonalized by the basis

$$\begin{pmatrix} \phi_{k,+} \\ \phi_{k,-} \end{pmatrix} = \frac{1}{\sqrt{2}} \begin{pmatrix} -\bar{\eta}_k & 1 \\ \bar{\eta}_k & 1 \end{pmatrix} \begin{pmatrix} p_{k_A} \\ p_{k_B} \end{pmatrix}; \quad \bar{\eta}_k = \sqrt{\frac{t_1 + t_2 e^{-ikd}}{t_1 + t_2 e^{ikd}}}. \tag{3.32}$$

Thus we find

$$H = -\bigoplus_{k=1}^{N} \begin{pmatrix} \phi_{k,+}^\dagger & \phi_{k,-}^\dagger \end{pmatrix} \begin{pmatrix} -\epsilon_k & 0 \\ 0 & \epsilon_k \end{pmatrix} \begin{pmatrix} \phi_{k,+} \\ \phi_{k,-} \end{pmatrix}; \quad \epsilon_k = t\sqrt{2}\sqrt{1 + \delta^2 + (1 - \delta^2)\cos(2ka)}, \tag{3.33}$$

and may choose states $\phi_{k,\pm}^\dagger |\emptyset\rangle = \frac{1}{\sqrt{2}} \left(\mp \bar{\eta}_k^* p_{k,A}^\dagger + p_{k,B}^\dagger \right) |\emptyset\rangle$ having energies $\pm\epsilon_k$, respectively.[4] Transforming back to the position basis, we find

$$\phi_{k,\pm}^\dagger |\emptyset\rangle = \frac{1}{\sqrt{2N}} \sum_{n=1}^{N} e^{-iknd} \left(\mp \bar{\eta}_k^* q_{n,A}^\dagger + q_{n,B}^\dagger \right) |\emptyset\rangle, \tag{3.34}$$

so that if we pull a factor of e^{ika} out of $\bar{\eta}_k^*$, we find

$$\eta_k = \sqrt{\frac{t_1 e^{ika} + t_2 e^{-ika}}{t_1 e^{-ika} + t_2 e^{ika}}}; \tag{3.35}$$

[4]Note that the creation operator uses the conjugate $\bar{\eta}_k^* = \bar{\eta}_k^{-1}$, equal to the reciprocal of $\bar{\eta}_k$ as it appears in Equation (3.32). This convention is meant to be consistent with the superscript daggers used for the creation operators.

so that the eigenstate

$$\phi^\dagger_{k,\pm}|\emptyset\rangle = \frac{1}{\sqrt{2N}}\sum_{n=1}^{N} e^{-ikn2a}\left(\mp e^{ika}\eta^*_k q^\dagger_{n,A} + q^\dagger_{n,B}\right)|\emptyset\rangle \tag{3.36}$$

$$= \frac{1}{\sqrt{2N}}\sum_{x=1}^{2N} e^{-ikxa}(\mp\eta^*_k)^{\theta_x} q^\dagger_x|\emptyset\rangle \tag{3.37}$$

clearly satisfies Bloch's theorem, where $\theta_x = (1-(-1)^x)/2$. Note that η^*_k is now equivalent to the coefficient $\mathcal{A}$ used by Ref. [108]. The general state amplitudes are thus

$$\gamma_k(x) = \langle x|\phi_{k,-}\rangle = \frac{1}{\sqrt{L}}e^{ikx}(\eta^*_k)^{\theta_x}. \tag{3.38}$$

Limit Cases of the Eigenstate

It is important that we check these equations against our intuition and limiting cases to reduce the chance of propagating mistakes through these calculations. Three limit cases with clear intuition come from three critical values of the dimerization, namely $\delta = 0,\ \pm 1$. We consider these cases now.

Critical Point ($\delta = 0$): As a test of sanity, let us check to see that we recover the familiar form of the regular lattice of spacing $a = 1$ in the case $\delta = 0$. At this critical point, the scalar η_k reduces to

$$\eta_k|_{\delta=0} = \sqrt{\frac{e^{ika}+e^{-ika}}{e^{-ika}+e^{ika}}} = 1 \tag{3.39}$$

and so the state amplitudes become

$$\langle n', i|\phi_{k,-}\rangle|_{\delta=0} = \frac{1}{\sqrt{L}}e^{-ikax}, \tag{3.40}$$

as they were for the uniform case, letting $x \in \{1, ..., L\}$ count the sites on the lattice.

Fully Dimerized ($\delta = 1$): For $\delta = 1$, inter-cell hopping is suppressed since $t_2 = 0$, so hopping only occurs within each unit cell via $t_1 = 2t$. Here, the scalar η_k reduces to

$$\eta_k|_{\delta=1} = \sqrt{\frac{e^{ika}}{e^{-ika}}} = e^{ika} \tag{3.41}$$

so that both sites in the unit cell share the same amplitude, indicating an even superposition of sites A and B.

Fully Dimerized ($\delta = -1$): Now for $\delta = -1$, the intra-cell hopping is suppressed since $t_1 = 0$, and hopping occurs only between adjacent unit cells via $t_2 = 2t$. The scalar η_k then becomes

$$\eta_k|_{\delta=-1} = \sqrt{\frac{e^{-ika}}{e^{ika}}} = e^{-ika}, \tag{3.42}$$

effectively shifting site each A into the previous unit-cell. This is equivalent to shifting the whole fully dimerized chain ($\delta = 1$) by a half-step, so that our boundary condition occurs between two coupled sites rather than two de-coupled sites, as above. Intuitively, this should affect the overall entanglement we measure, as our fixed subsystem boundary splits a strongly correlated mode within the unit cell at the periodic bound of the lattice.

Band Structure

Looking at the dispersion relation (3.33) in Fig. 3.5, we see that this model is gapped at half-filling, when all the occupied modes $|\phi_k\rangle$ have $\epsilon_k \leq 0$. The half-filled ground state is therefore $|\Phi_0\rangle = \prod_{k \leq k_F} \phi^\dagger_{k,-}|\emptyset\rangle$. According to Refs. [24, 23], this gapped state should exhibit area law scaling in its entanglement entropy when it is gapped (half-filled and $\delta \neq 0$), so we look to verify this prediction.

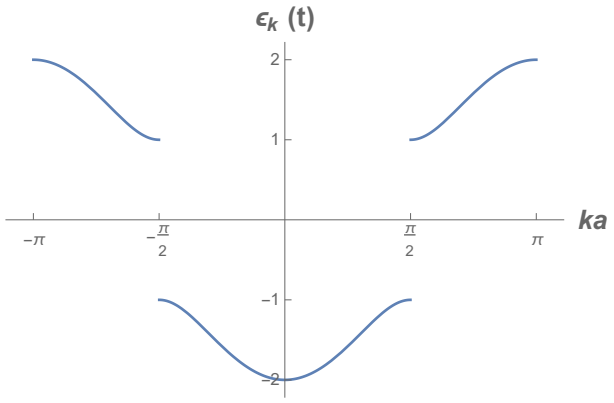

Figure 3.5: Dispersion relation for the SSH model taking $|\delta| = 0.5$. Notice the thermodynamic gap $\Delta_E \sim 4|\delta|$ at the Fermi points $|ka| = \pi/2$. The FBZ runs from $[-\pi/2, \pi/2)$ here, but is extended to intuitively partition the crystal momenta into the upper- and lower bands.

3.3.3 Topology in the SSH Model

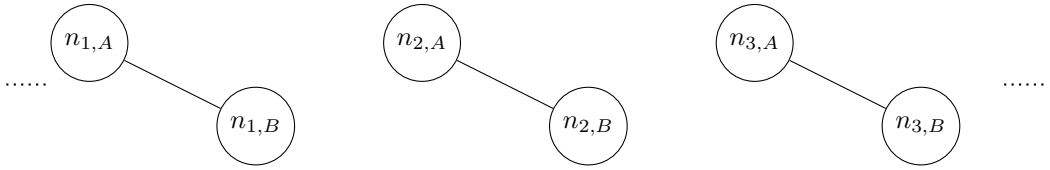

Figure 3.6: Illustration of trivial phase of the SSH model for $\delta = 1$. The energy eigenstates assume superposition within each unit cell for the whole lattice.

Literature has identified two distinct gapped topological phases in the SSH model: the trivial phase for $\delta > 0$, and a *symmetry protected topological (SPT)* phase for $\delta < 0$ [109, 108, 110]. These phases may be identified by their bulk-winding numbers, or equivalent *topological invariants* [109]. A topological invariant is formally an integer whose value does not change with respect to diffeomorphisms (smooth, or adiabatic transformations). In the SSH model, these transformations are ones that both preserve the symmetry of the Hamiltonian, and do not close the gap. For a fixed state of the Hamiltonian, we only need to consider the latter to study our topological phase, and use variation of δ as our adiabatic transformation (up to the critical point).

In the SSH model, a useful invariant for characterizing it is the number of edge modes

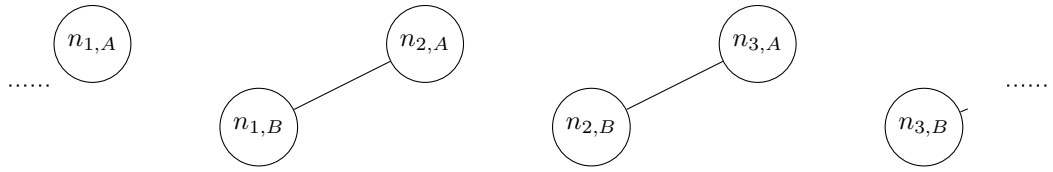

Figure 3.7: Illustration of topological phase of the SSH model for $\delta = -1$. The energy eigenstates assume superposition between neighbouring unit cells in the bulk, leaving unpaired sites at the edges of the chain which host the surface modes.

present, which is preserved by the chiral symmetry of the Hamiltonian [109]. Qualitatively, we may think of the edge modes as occupying the unpaired ends of the chain in the limit of full dimerization, leftover from the pairs of two-site superpositions within the bulk. Figure 3.6 shows the limit of full dimerization in the trivial case, where the eigenstates are given as superpositions over the two sites within each unit cell, and there are no unpaired modes. For the topological phase, Figure 3.7 shows the unpaired edge sites that host zero-energy surface modes, which have been recently observed in experiement [111].

With this model, we can watch for a phase transition, marked by the closing of the gap at critical point $\delta = 0$ as the system transitions between the trivial, and SPT phases [108]. This provides a simple toy model with which to explore signatures of topological order encoded within the entanglement entropy, and a curious link between topological matter and biological systems, as well.

Chapter 4

Numerical Methods

To see how the bipartite entanglement scales within a state, requires its evaluation across many partitions of a single lattice, motivating the use of numerical methods for efficiency. Given the state amplitudes $\gamma_k(x)$ for our system, we may obtain the entanglement spectrum and subsequent entanglement entropy in a few different ways. This chapter details the application of the techniques introduced in Chapter 2 to the systems defined in Chapter 3, and presents each method in terms of the numerical algorithm written into Python to return data [112]. Each method is later compared in terms of accuracy, domain, and efficiency.

4.1 Methods

The overview of our methodology for the calculation and characterization of the entanglement entropy scaling within these bipartite systems will be to first define a lattice geometry: including its size L, population F, set of mode amplitudes $\mathcal{M} = \{\gamma_k(x)\}$. The standard procedure is then to cycle through the series of contiguous partitionings $A = \{1, \cdots, \ell_A\} \subset L$ of the lattice and compute the spectrum $\{\lambda_i\}^A$ and associated entropy $S(A) = S(\ell_A)$ for each. The following methods are therefore presented and analyzed as algorithms taking in

the lattice geometry and partition size as input, and returning the entanglement spectrum as output $\mathfrak{A} : (\mathcal{M}, F, L, \ell) \to \{\lambda_i\}^A$.

4.1.1 Singular Value Decomposition

If we have a *pure state*

$$|\Psi\rangle = \sum_{a,b} M_{ab} |\Phi_a\rangle |\Phi_b\rangle \tag{4.1}$$

living in the joint Hilbert space $\mathcal{H}_A \otimes \mathcal{H}_B$, we may compute the entanglement spectrum via the SVD of the matrix M_{ab}. This can be done using the Python method *numpy.linalg.svd* [112, 113], which will return the SVD of a matrix $A = UDV^T$, an $m \times n$ matrix, in time $\mathcal{O}(m^2 n)$, where $m \leq n$[1]. Using this built-in method, the heavy-lifting, per sé, is then the construction of this matrix from the set of mode amplitudes $\mathcal{M} = \{\gamma_k(x)\}$.

To form M_{ab} one must compute the probability amplitudes associated to each composite mode $|\Phi_a\rangle|\Phi_b\rangle$. Particle conservation lets us partition the modes into groupings of subpopulations f for Alice, and $f^c = F - f$ for Bob. Let the set $X_a = \{a_1, \cdots, a_f, b_1, \cdots, b_{f^c}\} \subseteq \{1, \cdots, \ell_A\}$ identify the f occupied sites on Alice's side of the direct lattice, and let $X_b = \{b_1, \cdots, b_{f^c}\}$ identify the occupied sites on Bob's side. Lists of this form are easy to iterate through computationally, and have the added benefit of tracking where each particle is in the state.[2] Concatenation of the two lists then gives the set of occupations X_{ab} defining the pure state $|X_{ab}\rangle = |\Phi_a\rangle|\Phi_b\rangle$. Since we are tracking the occupations of the particles with this formalism, the amplitude M_{ab} must be determined via the Slater determinant to account for the particle statistics[3]

$$M_{ab} = |\Phi(X_{ab})|, \tag{4.2}$$

[1] Without loss of generality. If $m > n$, we simply use the transpose $VDU^T = A^T \in M_{n,m}$ and the complexity remains. In practice, $m \leq n$ is consistent with the iteration of our partition ℓ such that $\dim \mathcal{H}_A \leq \dim \mathcal{H}_B$.

[2] Note that if we are using the second-quantized formalism, these lists must be ordered to prevent double counting.

[3] There is no getting around it!

where $\Phi(X_{ab})$ is the matrix containing the amplitudes $\gamma_k(x)$ associated to a single particle with crystal momentum k found at the site $|x\rangle = q_x^\dagger|\emptyset\rangle$. For the state $|X\rangle = |x_1, \cdots, x_F\rangle$ at zero temperature, we have

$$M_X = |\Phi(X)| = \begin{vmatrix} \gamma_1(x_1) & \gamma_1(x_2) & \cdots & \gamma_1(x_F) \\ \gamma_2(x_1) & \gamma_2(x_2) & \cdots & \gamma_2(x_F) \\ \vdots & \vdots & \ddots & \vdots \\ \gamma_F(x_1) & \gamma_F(x_2) & \cdots & \gamma_F(x_F) \end{vmatrix}. \tag{4.3}$$

Equation (4.1) tells us which sets X_{ab} to consider, given the subspaces $\mathcal{H}_A$ and $\mathcal{H}_B$, fixed by the size of the lattice L, population F, and partition ℓ. Each of the sets X_{ab} define one element of the matrix M_{ab} that we are constructing, and we must enumerate each possible state $|\Phi_a\rangle|\Phi_b\rangle$ appearing in Equation (4.1) to obtain the full matrix. Thankfully, these states may be nicely grouped according to the number of fermions f occupying Alice's lab, which simultaneously fixes the number of fermions $f^c = F - f$ on Bob's side, so that the matrix M_{ab} is block anti-diagonal, with non-trivial blocks M^{f,f^c} corresponding to the pairs of complementary populations in the two labs. We may then fill out our matrix piecewise by iterating over the possible populations of Alice's lab $0 \leq f \leq \hat{F}$, where $\hat{F} = \min\{\ell, F\}$ is

the maximum possible occupancy of Alice's subsystem. Our matrix M_{ab} takes the form

$$M_{ab} = \begin{array}{c} \begin{matrix} [|b_j^F\rangle] & \cdots & |b_s^{f^c}\rangle & \cdots & |b_1^{f^c}\rangle & \cdots & [|b_1^{\hat{F}^c}\rangle] \end{matrix} \\ \begin{pmatrix} 0 & \cdots & 0 & \cdots & 0 & \cdots & M^{\hat{F},\hat{F}^c} \\ \vdots & \iddots & & & & \iddots & \vdots \\ 0 & & M_{1,s}^{f,f^c} & \cdots & M_{1,1}^{f,f^c} & & 0 \\ \vdots & & \vdots & \iddots & \vdots & & \vdots \\ 0 & & M_{r,s}^{f,f^c} & \cdots & M_{r,1}^{f,f^c} & & 0 \\ \vdots & \iddots & & & & \iddots & \vdots \\ M^{0,F} & \cdots & 0 & \cdots & 0 & \cdots & 0 \end{pmatrix} \end{array} \begin{matrix} [|a_i^{\hat{F}}\rangle] \\ \vdots \\ |a_1^f\rangle \\ \vdots \\ |a_r^f\rangle \\ \vdots \\ [|a^0\rangle] \end{matrix} , \tag{4.4}$$

where the upper indices f, f^c define the groupings, and the lower indices $r = r(f),\ s = s(f^c)$ count the specific arrangements of fermions in each lab given that grouping.

For each subpopulation f there are $\binom{\ell}{f}$ ways to arrange the fermions, so the dimension of M_{ab} is the same as $\mathcal{H}_A$, equal to the sum

$$\dim M_{ab} = \dim \mathcal{H}_A = \sum_{f=0}^{\hat{F}} \binom{\ell}{f}. \tag{4.5}$$

Similarly, the dimension of $\mathcal{H}_B$ is found using the complementary quantities

$$\dim \mathcal{H}_B = \sum_{f=0}^{\hat{F}} \binom{\ell^c}{f^c}. \tag{4.6}$$

The numerical approach will therefore be to cycle through the subspaces $\mathcal{H}_A|_f \subset \mathcal{H}_A$, and $\mathcal{H}_B|_{f^c} \subset \mathcal{H}_B$, pairing each mode $|\Phi_{a(f)}\rangle$ with all possible complements $|\Phi_{b(f^c)}\rangle$, and adding the amplitudes to our state matrix M_{ab}. Once we have the matrix M_{ab}, the *numpy.linalg.svd* method in Python is used to return the singular values [112, 113], whose squares constitute

the entanglement spectrum $\{\lambda_i\}^A$. This method uses the LAPACK routine *_gesdd*, which computes the SVD of a matrix $A \in M_{m,n}$ at cost $\mathcal{O}(m^2 n)$, for $m \leq n$ [113, 114]. In practice, we will find that $\dim \mathcal{H}_A < \dim \mathcal{H}_B$ since we will only take $1 \leq \ell \leq L/2$.

Algorithm: SVD

Given a lattice geometry $(\mathcal{M}, F, L)$ and a partition length ℓ, we employ Algorithm 1 to obtain the entanglement spectrum. The efficiency of this algorithm is limited by the complexity of the formation of M_{ab}. For every subpopulation $f \in [1, \hat{F}] \subset \mathbb{Z}$, there are $\binom{\ell}{f}$ modes on Alice's side to pair with $\binom{\ell^c}{f^c}$ modes on Bob's. Across all volumes and partitions, this number is upper bounded by $\binom{L/2}{L/4}^2$ pairings in the case of a half-filled and an equally split lattice of length L. The time to construct the matrix M_{ab} is then limited to the speed at which our computer can create, perform, and store the outputs of $\mathcal{O}(\binom{L/2}{L/4}^2)$ determinants. Each of these determinants is taken of a matrix $\Phi(X_{ab}) \in GL(F)$, where the cost to create $\Phi(X_{ab})$ will be the cost of calculating $\mathcal{O}(F^2)$ mode coefficients to fill out the matrix, plus the cost to take the determinant, which is $\mathcal{O}(F^3)$ through LU decomposition. For a fixed partitioning on a half-filled lattice of $F = L/2$ fermions, the complexity of this algorithm is thus bounded by the cost to create M_{ab} and the cost to decompose it

$$T(F) \sim \mathcal{O}\left(F/2\binom{F}{F/2}^2 (F^3 + F^2)\right) + \mathcal{O}\left(\left(\sum_f \binom{F}{f}\right)^3\right). \tag{4.7}$$

This does not look good for us, since factorial time, while slightly faster than exponential time, is still far from efficient. These calculations will thus be severely limited in the system size, unless clever short-cuts are found. Further, the large number of operations involved in this algorithm give lots of room for machine precision error to accumulate throughout the

calculation, which will also limit the size of system that we may handle accurately.

Data: Given the set of mode amplitudes $\mathcal{M}$, system volume F, L, and partition length ℓ;

Result: Calculate M_{ab} and obtain entanglement spectrum via SVD.

for *fixed partition* ℓ **do**

Define: $da = \dim \mathcal{H}_A = \sum_f \binom{\ell}{f}$; $\quad db = \dim \mathcal{H}_B = \sum_f \binom{\ell^c}{f^c}$;

initialize: M_{ab} = np.zeros((*da*, *db*),dtype=np.complex);

Track column; starting top left: $\mathfrak{c} = db - 1$;

initialize row $r = 0$;

for *the number of fermions* f *in Alice's lab:* **do**

for *every arrangement* $|\Phi_{a(f)}\rangle$ *of* f *fermions over Alice's* ℓ *sites:* **do**

reset the column index $c = \mathfrak{c}$;

for *each complement state* $|\Phi_{b(f^c)}\rangle$*:* **do**

Concatenate the substates into $|X_{ab}\rangle = |\Phi_{a(f)}\rangle|\Phi_{b(f^c)}\rangle$;

Create the matrix $\Phi(X_{ab})$ using the set $\mathcal{M} = \{\gamma_k(x)\}$;

Compute and store the state amplitude $M_{ab} = |\Phi(X_{ab})|$;

Change the column: $c -= 1$;

end

Change the row: $r += 1$;

end

Save set column index to start the next block $\mathfrak{c} = c$;

end

Take the SVD and store the singular values $\sqrt{\lambda_i}$;

Square the singular values to obtain the entanglement spectrum λ_i;

Print entanglement spectrum

end

Algorithm 1: $\mathfrak{A}^{SVD} : (H, F, L, \ell) \to \{\lambda_i\}^A$.

4.1.2 Entanglement Spectrum via the Reduced Density Matrix

If our state is mixed, such that it must be described by a density matrix rather than a pure state vector, we'll need to take the partial trace over Bob's system to arrive at Alice's reduced density matrix

$$\rho^A = \mathrm{Tr}_B[\rho^{AB}] = \sum_i \lambda_i |i_a\rangle\langle i_a|, \tag{4.8}$$

whose eigenvalues $\{\lambda_i\}$ are the squares of the Schmidt spectrum. To construct the RDM, we might first construct the full DM and partial trace, but will find that we can save time by grouping states with the same subpopulations as before.

Since our subsystems are defined in position space, it is convenient to express our DM in the position basis. Let

$$|\Phi_{X_\alpha}\rangle = \prod_{x\in X_\alpha} q_x^\dagger |\emptyset\rangle \tag{4.9}$$

be the state of $F = |X_\alpha|$ fermions occupying the sites $X_\alpha = \{x_{\alpha_1}, \cdots, x_{\alpha_F}\}$ on the direct lattice; and let

$$|\Psi_\alpha\rangle = \sum_X M_X^{(\alpha)} |\Phi_X\rangle \tag{4.10}$$

be a pure state of our system, where the index α is meant to index the pure states found within the generalized mixed ensemble

$$\rho = \sum_\alpha p_\alpha |\Psi_\alpha\rangle\langle\Psi_\alpha|. \tag{4.11}$$

So long as our states are pure, our ensemble has only one term $\rho = |\Psi\rangle\langle\Psi|$, taking the form

$$\rho^{AB} = \sum_{X,Y} M_X M_Y^\dagger |X\rangle\langle Y| = \sum_{a,a',b,b'} M_{ab} M_{a'b'}^\dagger |\Phi_a\Phi_b\rangle\langle\Phi_{a'}\Phi_{b'}|, \tag{4.12}$$

where $M_{ab} = |\Phi(X_{ab})|$ as before. In matrix notation, our pure state DM looks like

$$\rho^{AB} = \begin{array}{c} \begin{array}{cccccc} |\Phi_a\rangle|\Phi_b\rangle & \cdots & |\Phi_{a'}\rangle|\Phi_b\rangle & \cdots & |\Phi_{a'}\rangle|\Phi_{b'}\rangle & \cdots \end{array} \\ \begin{pmatrix} M_{ab}M_{ab}^\dagger & \cdots & M_{a'b}M_{ab}^\dagger & \cdots & M_{a'b}M_{ab}^\dagger & \cdots \\ \vdots & \ddots & \vdots & \ddots & \vdots & \\ M_{ab}M_{a'b}^\dagger & \cdots & M_{a'b}M_{a'b}^\dagger & \cdots & M_{a'b}M_{a'b}^\dagger & \cdots \\ \vdots & \ddots & \vdots & \ddots & \vdots & \\ M_{ab}M_{a'b'}^\dagger & \cdots & M_{a'b}M_{a'b'}^\dagger & \cdots & M_{a'b}M_{a'b'}^\dagger & \cdots \\ \vdots & \ddots & \vdots & \ddots & \vdots & \ddots \end{pmatrix} \end{array} \begin{array}{c} \\ \langle\Phi_a|\langle\Phi_b| \\ \vdots \\ \langle\Phi_{a'}|\langle\Phi_b| \\ \vdots \\ \langle\Phi_{a'}|\langle\Phi_{b'}| \\ \vdots \end{array} . \tag{4.13}$$

Taking the partial trace, we measure out Bob's degrees of freedom, effectively reweighting Alice's modes

$$\begin{aligned} \rho^A &= \sum_{\mathbf{b}\in B} (\mathbb{1}\otimes\langle\mathbf{b}|) \left(\sum_{a,a',b,b'} M_{ab}M_{a'b'}^\dagger |ab\rangle\langle a'b'| \right) (\mathbb{1}\otimes|\mathbf{b}\rangle) \\ &= \sum_{a,a'\in A} \left(\sum_{b\in B} M_{ab}M_{a'b}^\dagger \right) |a\rangle\langle a'| \end{aligned} \tag{4.14}$$

according to their connections to Bob's states. We thus find that the construction of Alice's RDM involves the enumeration of the three basis sets $\{|a\rangle\}, \{|a'\rangle\}, \{|b\rangle\}$.

As before, our reduced density matrix is neatly partitioned into groupings of subpopulation f. Observe that tracing out a state $|b_{f^c}\rangle = q_{x_1}^\dagger \cdots q_{x_{f^c}}^\dagger |\emptyset\rangle$ with $f^c = F - f$ fermions in Bob's lab will annihilate any state $|b'\rangle$ containing a different number of fermions. Therefore, all terms in Equation 4.14 are such that modes $|a\rangle$ and $\langle a'|$ contain the same number of fermions f. Alice's reduced density matrix is therefore block diagonal

$$\rho^A = \bigoplus_{f=0}^{\hat{F}} \rho_f^A, \tag{4.15}$$

where each *reduced density block (RDb)* ρ_f^A describes the states of f particles in Alice's lab. This is good news for our algorithm, as the diagonalization of ρ^A is conveniently partitioned into the diagonalizations of each ρ_f^A independently.

Algorithm: RDM

Algorithmically, the elements of the RDM are computed by iterating over the possible configurations of Alice, Bob, and Alice again to compute the coefficient $M_{ab}M_{a'b}^\dagger$ in Equation 4.14. For a set lattice length L, population $F = L/\zeta$, and partition ℓ, the entanglement

spectrum is computed using Algorithm 2.

Data: Given the lattice geometry $(\mathcal{M}, F, L)$ and partition length ℓ;

Result: Construct ρ^A and extract the entanglement spectrum $\{\lambda_i\}$.

for *Define partition* $1 \leq \ell \leq L/2$*:* **do**

  for *the number of fermions* f *in Alice's lab:* **do**

    set $d = \binom{\ell}{f}$;

    initialize: ρ_f^A = np.zeros((d, d),dtype=np.complex);

    for *every arrangement* $|\Phi_{a(f)}\rangle$ *of* f *fermions over Alice's* ℓ *sites:* **do**

      for *each complement state* $|\Phi_{b(f^c)}\rangle$*:* **do**

        Concatenate to form $|X_{ab}\rangle = |\Phi_{a(f)}\rangle|\Phi_{b_{f^c}}\rangle$;

        Compute the amplitude M_{ab} of mode X_{ab};

        for *each arrangement in Alice's lab again* $|\Phi_{a'(f)}\rangle$*:* **do**

          Concatenate to form $\langle X_{a'b}| = \langle\Phi_{a'(f)}|\langle\Phi_{b_{f^c}}|$;

          Compute the amplitude $M^\dagger_{a'b}$ for the mode $X_{a'b}$;

          Add the product $M_{ab}M^\dagger_{a'b}$ to the element $(\rho_f^A)_{a,a'}$;

        end

      end

    end

    Diagonalize ρ_f^A and append eigenvalues λ_i to the entanglement spectrum;

  end

  # Print spectrum.

end

Algorithm 2: $\mathfrak{A}^{RDM} : (H, F, L, \ell) \to \{\lambda_i\}^A$.

The cost of the Algorithm 2 is largely limited by the expensive construction of ρ_f^A. As before, the dimension of ρ_f^A is given by the dimension of the related eigenspace

$$\dim \mathcal{H}_A|_f = \binom{\ell}{f}, \tag{4.16}$$

giving $\binom{F}{F/2}$ in the worst case. Compared to the SVD approach, we iterate through this eigenspace twice for each of Bob's states, so the construction of the largest ρ_f^A for a half-filled lattice of F fermions requires the computation of $\mathcal{O}(\binom{F}{F/2}^3)$ determinants $|\Phi(X)| : GL(F) \to \mathbb{C}$. The good news here is that compared to the SVD, our block decomposition of ρ^A speeds up its diagonalization: instead of diagonalizing $\rho^A \in GL(\dim \mathcal{H}_A)$ we can diagonalize the smaller blocks $\rho_f^A \in GL(\dim \mathcal{H}_A|_f)$ more efficiently, evidenced by the standard inequality

$$\sum_{i \in I} x_i^n \leq \left(\sum_{i \in I} x_i \right)^n \tag{4.17}$$

for all sets of $x_i \geq 0$, with equality only when $x_i = 0,\ \forall i \in I$, or when $n = 1$. For a half-filled lattice of F fermions, the runtime to compute the entanglement spectrum for any given partitioning is thus bounded by the time to construct each block ρ_f^A and the cost to diagonalize it

$$T(F) \sim \sum_{f=0}^{\hat{F}} \left[\mathcal{O}\left(\binom{F}{F/2}^3 (F^3 + F^2) \right) + \mathcal{O}\left(\binom{F}{f}^3 \right) \right]. \tag{4.18}$$

Compared to the SVD algorithm (Equation 4.7), we see that it is faster to diagonalize the disjoint blocks ρ_f^A than to decompose the matrix M_{ab}, however, each block requires exponentially more operations to construct, compared to M_{ab}^f. While the RDM method is generally less efficient than the SVD method, it is necessary if one is to calculate entanglement measures of mixed states; and while this is not the focus of this work, it is still worth mentioning.

4.1.3 The Entanglement Hamiltonian

In the special case of a Gaussian state,[4] a more efficient method to calculate the von Neumann entropy within the ground state of a fermionic hopping model is through the calculation of

[4]Gaussian states are those states in thermal equilibrium given a quadratic Hamiltonian, either bosonic, or fermionic.

the *single-body correlation functions*

$$Q_{x,y} = \langle q_x^\dagger q_y \rangle, \tag{4.19}$$

from which the state's density matrix is determined [115]. In particular, the $\ell \times \ell$ block $C_{i,j}$ within the full $L \times L$ correlation matrix Q is tied to the reduced density matrix ρ^A for $A = \{1, \cdots, \ell\} \subset L$, through the so-called *entanglement Hamiltonian* H_A [116, 115, 117, 118], defined strictly on the subsystem:

$$H_A = \sum_{i,j}^{\ell} h_{ij} q_i^\dagger q_j, \tag{4.20}$$

such that

$$\rho^A = \mathcal{K} \exp\left(- \sum_{i,j}^{\ell} h_{ij} q_i^\dagger q_j \right), \tag{4.21}$$

for an appropriate scalar $\mathcal{K}$ to normalize. The entanglement Hamiltonian $\mathbf{h}$ inherits its hermicity from ρ^A and is therefore diagonalizable by a change of basis. Let $f_l = \sum_k U_{lk} c_k$ be the basis of fermionic operators diagonalizing H_A, then

$$\rho^A = \mathcal{K} \exp\left(- \sum_{l=1}^{\ell} \varepsilon_l f_l^\dagger f_l \right), \tag{4.22}$$

so that the spectrum of ρ^A is directly related to the entanglement spectrum $\lambda_j = e^{-\varepsilon_j}$.

For Gaussian states, the entanglement Hamiltonian $\mathbf{h}$ is related to the *truncated* correlation matrix $\mathbf{C}$ [115] considering only the correlations within Alice's subsystem

$$\mathbf{h} = \ln[(1 - \mathbf{C})/\mathbf{C}]; \tag{4.23}$$

and likewise for their eigenvalues

$$\varepsilon_l = \ln[(1 - z_l)/z_l]. \tag{4.24}$$

From the eigenvalues z_l of the $\ell \times \ell$ truncated correlation matrix $C_{i,j}$, the von Neumann entropy is obtained by summing of the binary entropy $H_2(x) = -x \log x - (1 - x) \log(1 - x)$ for each eigenvalue of the correlation matrix [119]

$$S(\rho^A) = \sum_{l=1}^{\ell} H_2(z_l), \tag{4.25}$$

and computing the entanglement using this method thus boils down to the formation and diagonalization of the truncated correlation matrix C_{ij}.

For the pure state

$$|\Psi\rangle^{AB} = \prod_{k \in \kappa} p_k^\dagger |\emptyset\rangle; \quad p_k^\dagger = \sum_{x \in L} U_{kx} q_x^\dagger, \tag{4.26}$$

with fixed crystal momenta $\kappa = \{k_1, \cdots, k_F\}$, Equation (4.19) takes on a remarkably simple form. If the diagonal basis $|p_k\rangle$ is related to the position basis $|q_x\rangle$ by the unitary transformation U_{kx}, we find

$$\begin{aligned} Q_{x,y} = \langle q_x^\dagger q_y \rangle &= \langle \emptyset | p_{k_F} \cdots p_{k_1} \left(q_x^\dagger q_y \right) p_{k_F}^\dagger \cdots p_{k_1}^\dagger | \emptyset \rangle & (4.27) \\ &= \langle \emptyset | p_{k_F} \cdots p_{k_1} \left(\sum_{ij} U_{ix}^\dagger U_{jy} p_i^\dagger p_j \right) p_{k_F}^\dagger \cdots p_{k_1}^\dagger | \emptyset \rangle & (4.28) \\ &= \sum_{i,j} \left(U_{ix}^\dagger U_{jy} \right) \langle \emptyset | p_{k_F} \cdots p_{k_1} \left(p_i^\dagger p_j \right) p_{k_F}^\dagger \cdots p_{k_1}^\dagger | \emptyset \rangle & (4.29) \\ &= \sum_{i,j} U_{ix}^\dagger U_{jy} \delta_{ij} \delta_{ik_l}. & (4.30) \end{aligned}$$

For our models, the unitary transformation is given by the eigenfunctions of our Hamiltonian

$U_{kx} = \gamma_k(x)$. Then the correlation matrix

$$Q_{x,y} = \langle q_x^\dagger q_y \rangle = \sum_{k \in \kappa} \gamma_k^\dagger(x) \gamma_k(y) \tag{4.31}$$

may be constructed from our set $\mathcal{M} = \{\gamma_k(x)\}$ in polynomial time!

To look at the entanglement between the two sides of the lattice, we need one of the reduced density matrices. For these Gaussian states, the RDM is completely determined by the associated correlation functions $C_{i,j}$, where site indices i and j are restricted to Alice's lab, such that the correlation functions may be found from ρ^A

$$C_{i,j} = \mathrm{Tr}[\rho^A q_i^\dagger q_j], \tag{4.32}$$

by design. In the context of Equation (4.31), this restricted correlation matrix is simply the $\ell \times \ell$ block pertaining to Alice's sites in the full state correlation matrix

$$Q_{x,y} = \begin{matrix} \\ \\ \\ \\ \end{matrix} \begin{matrix} \leftarrow & \ell & \rightarrow & \\ \end{matrix} \begin{pmatrix} C_{1,1} & \cdots & C_{1,\ell} & \cdots \\ \vdots & \ddots & \vdots & \\ C_{\ell,1} & \cdots & C_{\ell,\ell} & \\ \vdots & & & \ddots \end{pmatrix} \begin{matrix} \uparrow \\ \\ \ell \\ \\ \downarrow \end{matrix}, \tag{4.33}$$

where we only have to compute $\mathcal{O}(F^3)$ elements; none of which are determinants!

$$T(F) \sim \mathcal{O}\left(F^3\right). \tag{4.34}$$

Algorithm: Entanglement Hamiltonian

The numerical method designed to compute the entanglement entropy of a given lattice geometry $(\mathcal{M}, F, L)$ is outlined in Algorithm 3. It is the most efficient of our methods, by far, as it runs in polynomial time with the size of our lattice, avoiding combinatoric loops altogether. This efficiency proves advantageous when probing the thermodynamic limit of our lattices and considering larger systems. Further, as this method requires the least number of operations per partition, we should expect it to be the most precise, as it should be the least affected by accumulated machine error.

Data: Given the lattice geometry $(\mathcal{M}, F, L)$ and partition length ℓ;

Result: Compute the von Neumann entropy $S(A)$.

for *Define partition* $1 \leq \ell \leq L/2$*:* **do**

  initialize $C_{i,j}$ = np.zeros((ℓ, ℓ), dtype=np.complex);

  for *row index* $1 \leq i \leq \ell$*:* **do**

    for *column index* $1 \leq j \leq \ell$*:* **do**

      for *all occupied levels* $k \in \{k_1, \cdots, k_F\}$*:* **do**

        Add term $C_{i,j} \mathrel{+}= \gamma_k^\dagger(i)\gamma_k(j)$

      end

    end

  end

  Diagonalize $C_{i,j}$ to find $\{\zeta_l\}$;

  Compute vN entropy $S(\ell) = \sum_l H_2(\zeta_l)$;

  # Print $(\ell, S(\ell))$.

end

Algorithm 3: $\mathfrak{A}^{CLM} : (\mathcal{M}, F, L, \ell_A) \to S(\ell_A)$.

Chapter 5

Simulations

5.1 Testing the Algorithms

Before going on to use the developed script, its accuracy must be justified by way of tests against analytical predictions and physical reasoning. This section presents the sanity checks that each of the methods must pass in order to be used for study. To save space, we present these tests in the case of the Bravais lattice using the entanglement Hamiltonian subroutine given in section 4.1.3, and note that similar results were found using the other two methods, and for the SSH model. Since entanglement Hamiltonian subroutine is the most efficient of the presented methods, we use it as a benchmark for the numerical precision of our computation, with the most limited accumulation of machine precision errors out of the three methods given.

5.1.1 Translational Symmetry

As we are using crystal momentum as the quantum number of our system, our calculations must exhibit the corresponding translational symmetry we expect our lattice to hold. This symmetry is confirmed manually by adding a constant shift to each of the sites in the array

$X = \{x_1, \cdots, x_F\}$ when calculating the eigenfunctions $\gamma_k(x)$. The resulting entropies of our shifted system $\gamma_k(x+s)$ are compared to a controlled case ($s = 0$) and shown in Figure 5.1. That the curves appear to be the same for the fixed and shifted systems bodes well for the

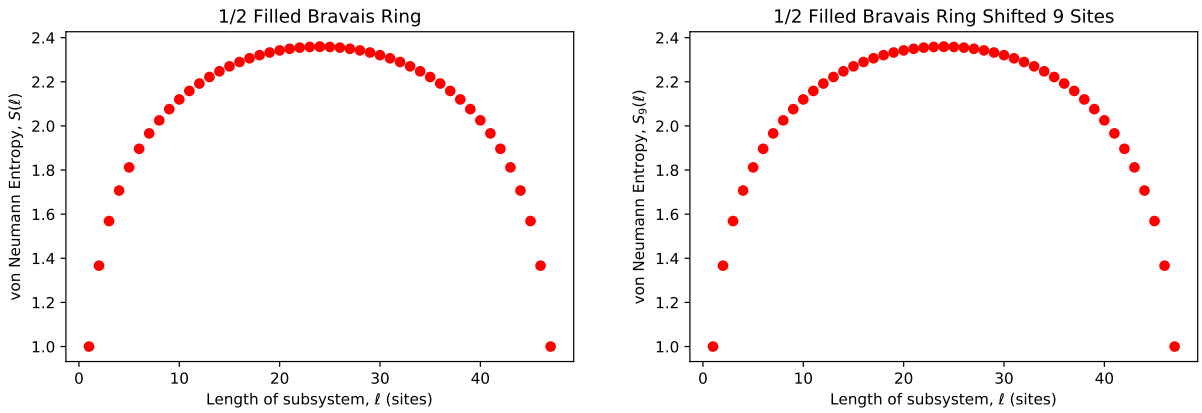

Figure 5.1: Translational symmetry exhibited by the algorithm in the similarity of the entropy curves for a standard lattice (left) and the same system shifted by $s = 4$ lattice sites (right).

translational invariance of our model. For a more quantitative comparison, we might ask what the difference in entropies is between a point on the fixed lattice and its equivalent point on the shifted lattice. This comparison is plotted in Figure 5.2 below, where we see a difference in the entropy comprable to the systematic error accumulated over thousands of computations using the 64-bit floats in Python [112].

5.1.2 Parity Symmetry

Parity symmetry of the entanglement is inherited from the finite size of our lattice. Since we are considering partitions into complement subsystems A and $B = A^c$, the larger we make one, the smaller the other will be. Then one should expect the entanglement between the two regions to be symmetric under a relabelling of A as B and vice-versa. This symmetry is exhibited in Figure 5.3, where we see a reflective symmetry about the halfway point in both the qualitative and quantitative plots. Further, the quantitative plot of the difference

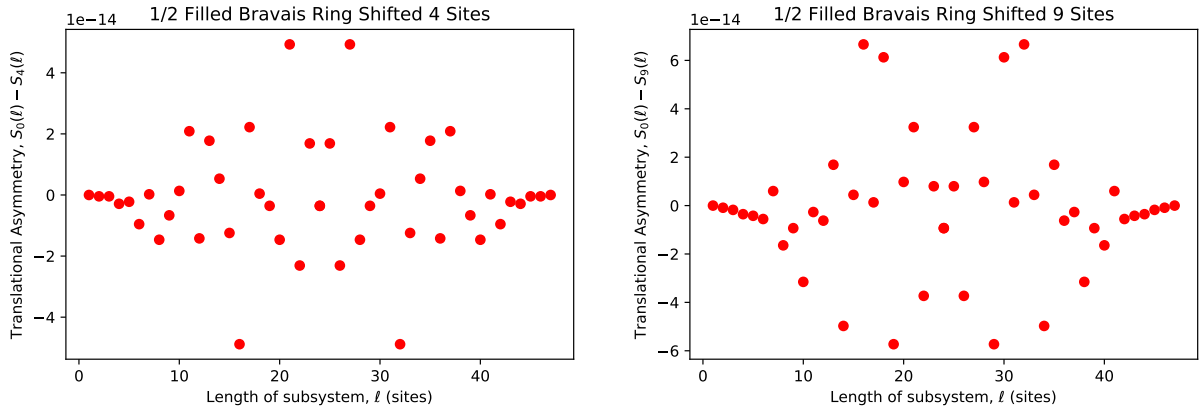

Figure 5.2: Magnitude of the translational asymmetry found in the algorithm for a given lattice size and shift.

in entropy for complementary partitions ℓ and $L - \ell$ is upper bounded by less than one part in a trillion; of comparable magnitude to the values of translational asymmetry. Having

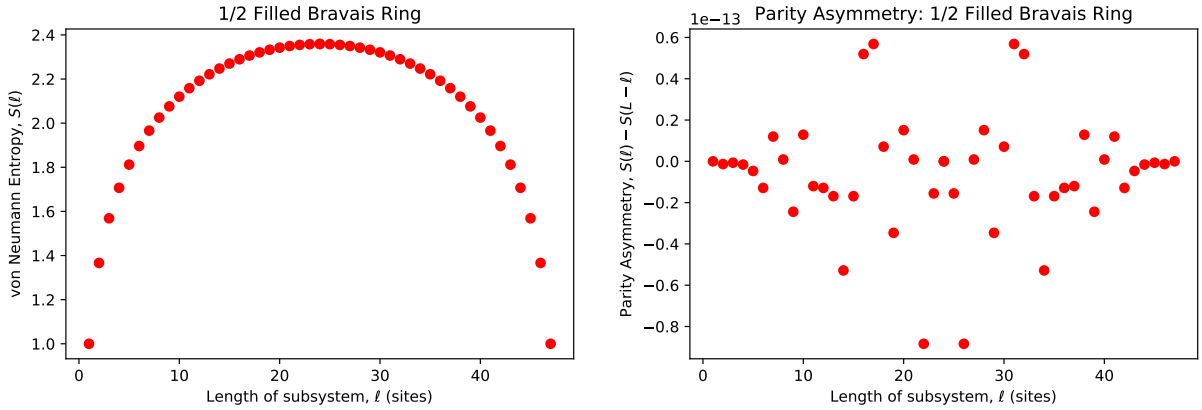

Figure 5.3: Parity symmetry exhibited by the algorithm in the symmetry of the entropy curve (left) and the difference in entropies between mirror-partitions (right).

confirmed that our script obeys parity, we can thus expedite these calculations (adding negligible error) by computing only up to half of the chain length and mirroring the results onto the other half. In actuality, we are mostly interested in a subset of the first half of a finite chain anyway, since the thermodynamic scaling is naturally disrupted by this parity symmetry.

5.1.3 Particle-Hole Symmetry

The finite nature of our systems also spur a symmetry in our quantum state encodings, deriving from the choice to either count the filled- or empty sites on the lattice. Invariance under the identification of one with the other is called *particle-hole symmetry*, and is expected in our finite systems thanks to our particle conserving Hamiltonian. Particle-hole symmetry of the model is confirmed by checking that the script produces identical results for complementary sets of densities – whether there are F particles on L sites, or $(L - F)$ particles on the same lattice of L sites. Such comparison is presented in Figure 5.4, demonstrating particle-hole symmetry to similar precision as the two others above.

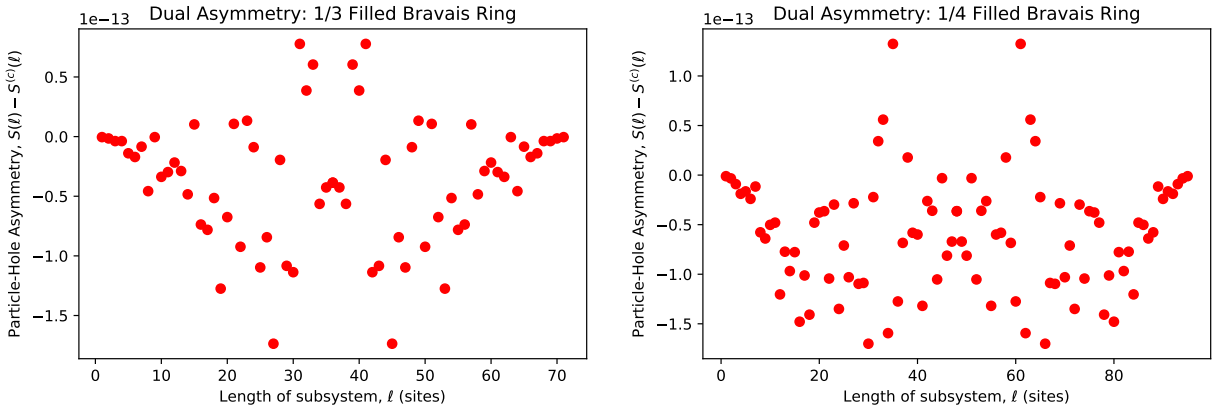

Figure 5.4: Particle-Hole asymmetry measured by taking the difference in entropies for each partition on a lattice of F fermions on L sites and the same lattice with $L - F$ fermions. Computed via the correlation matrix for lattices of $F = 24$ fermions at 1/3 filling (left) and 1/4 filling (right).

5.1.4 Precision of the Algorithm

We can use the observed asymmetry to give an approximation of the uncertainty of these calculations. On paper, we expect perfect symmetry, and can thus interpret the non-zero asymmetries shown in Figures 5.2, 5.3, 5.4 as the result of accumulated machine error. Since we are measuring the asymmetry using the difference entanglement entropy, we can upper-

bound the precision of our calculation by twice the greatest asymmetry for the given lattice size. For Figures 5.2, 5.3, 5.4, the asymmetry is on the order of 10^{-13}, for unit-scale entropies. As such, we needn't worry about it too much.

5.2 Comparison of the Methods

With three methods given for how to compute the entanglement entropy of a given system state, we should like to know the advantages and limitations of each. The methods are thus compared by way of their computational speed, accuracy, and limitations regarding the physical systems that support them.

Support of each method

As mentioned in the previous chapter, not all methods will be supported for the types of systems one might like to study. For instance, we know that density matrices are required to properly describe mixed states, and so the SVD is not supported on these systems. Similarly, the computational advantage of the correlation matrix derives from the pure state form of a fermionic ground state, and so again, mixed (including thermal) ensembles are not properly represented by this algorithm. Rather, extensions to the method must be employed, such as that presented in Ref. [120], for quadratic Hamiltonians in general. Since this thesis focuses on the ground states of fermionic hopping models, we may use any of the above algorithms. We then consider each based on their relative accuracy and computational efficiency below.

Relative Precision

Each of these methods are exact in theory, however, in practice, the more operations required by each method, the more we should expect its precision to fall as machine error accumulates. Further, comparing the output entropies of each method will warn us to any

problems in implementation, should the discrepancies be greater than can be explained by accumulated errors. The accuracy of each method is measured as its discrepancy with respect to the correlation matrix method, presented in Figure 5.5. We see that both the SVD and RDM subroutines appear to deviate from the entropy calculated through the correlation matrix. The logarithmic scale in the right panel of Fig 5.5 suggests that this discrepancy is tending to a exponential trend, which may be explained by the exponentially many number of computations required for these methods compared to the CLM, on paper. For such small systems, these discrepancies remain negligible, although the trend towards exponential scaling implies the RDM and SVD methods may be less reliable for systems sufficiently large.

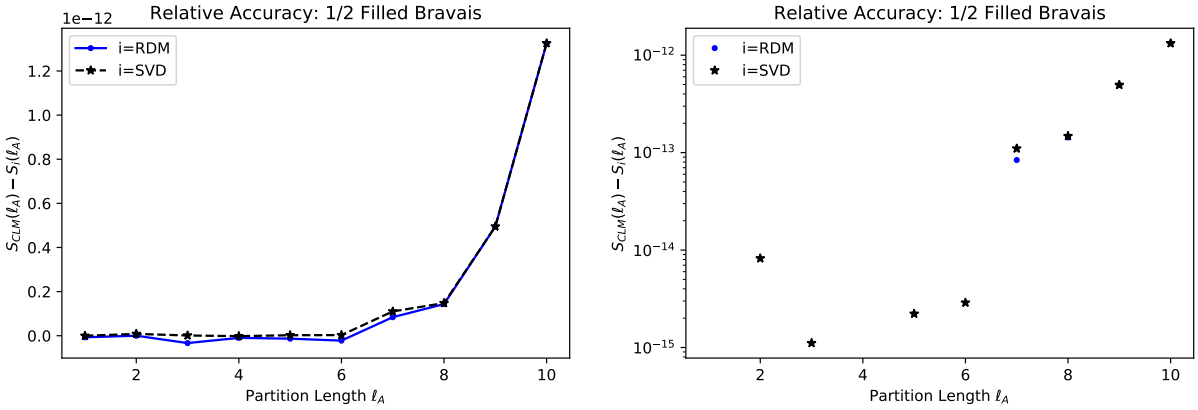

Figure 5.5: Comparison of the relative accuracy of the different methods for calculating the entanglement entropy given the three methods detailed above. The entropies obtained from the SVD and RDM methods are compared to the entropy calculated via the correlation matrix, and plotted against the partition size for a half-filled lattice populated by $F = 10$ fermions. We see the relative difference in entropy grow consistently for both the SVD and RDM, following an apparent exponential trend in the partition length.

Computational Efficiency

As we can see from the complexity of each algorithm, we should expect the Correlation Matrix to fare the best, given that the method is supported by our lattice. This is clear for

ground, and other pure states, however, we'll need to be a bit more clever for mixed/thermal states [120]. To measure the efficiency of each computation, let us use the partial trace method as the benchmark, since it is the most computationally expensive on paper.

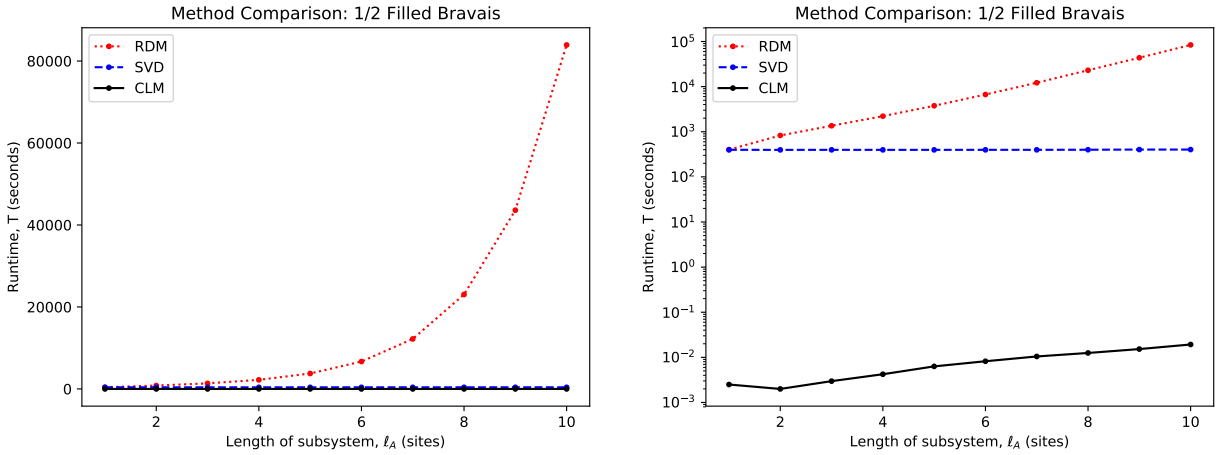

Figure 5.6: Comparing the clocked runtimes of the three different methods for calculating the entanglement entropy given above. Using a half-filled Bravais lattice populated by $F = 10$ fermions we see that the correlation matrix is easily the most efficient by roughly five orders of magnitude.

The runtime of each subroutine was obtained by writing a stopwatch function into the script to record the difference in clock times between the initial call to the method and a written print statement returning the entropy. Figure 5.6 shows these runtimes as a function of the partition length, for a fixed lattice of $F = 10$ fermions. The total runtime to compute the scaling of the lattice will be the sum of each data point for the method employed, and we see that the most efficient is clearly the correlation matrix method, by a few orders of magnitude. Further, the RDM and CLM curves both appear consistent with the time cost stated in the previous chapter. Comparing the runtime for $\ell = 10$ and $\ell = 1$, the CLM has taken roughly ten times as long for the larger subsystem, consistent with the polynomial scaling given (4.34), whereas the RDM has taken roughly a thousand times longer for the large system, consistent with the thrice-factorial cost (4.18). That the runtime of the SVD

appears to assume constant value throughout suggests that the stopwatch function failed to account for all processes involved in the calculation, as the stated runtime underestimates both the expected time cost (4.7), and the time one would attest from running the script themselves. Another timing method must therefore be employed to accurately time the SVD method.

5.3 Entanglement Scaling and Phase Characterization

The algorithms may now be employed as reliable tools for the calculation of entanglement entropies of quantum systems. Having identified the use correlation matrix as the most efficient method for our calculation, we employ it to probe the quantum phases of matter supported by our ground state systems.

5.3.1 Gapless Lattice: The Bravais Chain

Consider the tight binding model on the 1D Bravais lattice (3.19), whose dispersion relation is thermodynamically gapless across the entire FBZ (Figure 3.3). For these states, a logarithmic violation of the entanglement area law is expected, indicative of long-range quantum correlations. In particular, the vN entropy $S(\ell_A)$ defined for a contiguous subsystem $\ell_A \subset L$ of a one-dimensional lattice in the thermodynamic limit is expected to grow with the subsystem size, bounded by

$$c_- \log \ell_A \leq S(\ell_A) \leq c_+ \log^2(\ell_A), \tag{5.1}$$

with constants $c_\pm$ determined by the Fermi surface [25].

On the other hand, the same model on a finite lattice is known to find a maximum in its entropy for an equal partitioning $\ell_A = L/2 = \ell_B$, due to parity symmetry (Figure 5.3).

Thus, the logarithmic correction (5.1) must break-down near the centre of the lattice, and we cannot assume the thermodynamic limit here. Then, to use apply Wolf's analytical result to probe for gapless quantum phases more generally, we'll need to know how the thermodynamic approximation breaks down for finite-sized systems, as any numerical model used to study a quantum system is necessarily of finite extent.

Finite System Size

To compare our finite systems to Wolf's analytical result, we compute $S(\ell_A)$ for a variety of subsystem lengths and fit to a power law

$$S(\ell_A) \sim (\log \ell_A)^{\mathfrak{x}}, \tag{5.2}$$

checking that the logarithmic power satisfies Wolf's bounds: $1 \leq \mathfrak{x} \leq 2$. Given the parity symmetry in our systems, this fit must be limited to partitions $\ell_A \ll L$, coherent with the approximation made in Wolf's derivation. Therefore, we ask: for what fraction of the lattice $\mathfrak{f} = \ell/L$ (if any) does the thermodynamic approximation $\ell \ll L$ hold? Call this block $\ell_{\mathfrak{f}} = \{1, \cdots, \mathfrak{f}L\} \subset \ell_A$ the *thermodynamic regime* of the finite lattice if the entanglement scaling here proves sufficiently removed from finite-size parity effects.

Plotting the fit power $\mathfrak{x}$ against the fractional fit depth $\mathfrak{f}$, we look for convergence in the fit as indication for where on the entanglement trends consistently. The value $\mathfrak{f}_c$ for which the power-law fit (5.2) is consistent in $\mathfrak{x}$ is then assumed sufficiently removed from the finite-size effects to be tested against the thermodynamic approximation $\ell_c \ll L$. Figure 5.7 shows how the logarithmic power $\mathfrak{x}$ varies with the fractional choice of partitioning $\mathfrak{f}$ for fixed lattices of $F = 200$ fermions, at half- and third-fillings. In both cases, the trend is seen to flatten off around $\mathfrak{f} = 0.1$, although a spike is seen as well towards the left end, especially in the third-filled case. While this feature appears to be trending towards Wolf's bounds, it is not clear

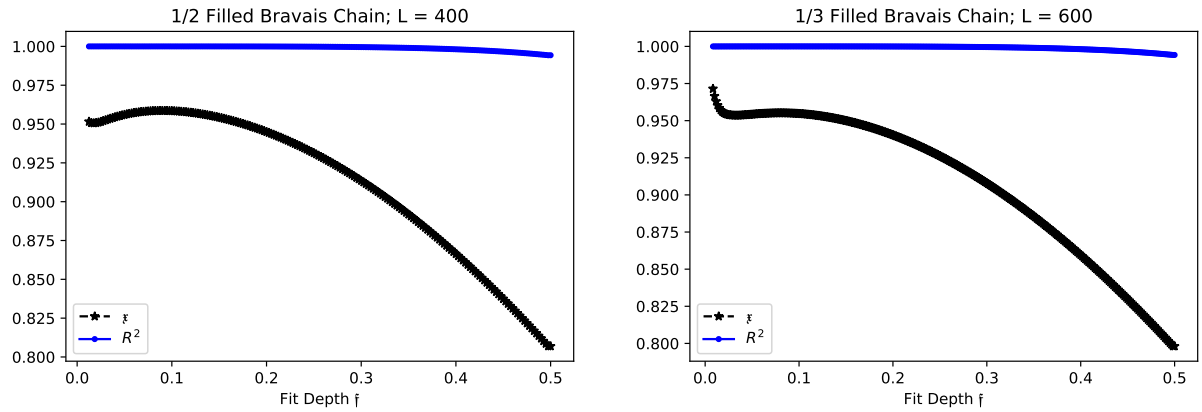

Figure 5.7: For two fixed lattice systems of $F = 200$ fermions, the logarithmic power $\mathfrak{x}$ and determination coefficient R^2 are plotted against the fit depth $\mathfrak{f}L$. As the fraction $\mathfrak{f}$ decreases, the fit power is seen to saturate around $\mathfrak{f} \approx 0.1$, but does not exceed unity for either system plotted.

that these data are sound, as these fits average a very limited number of points. Instead, let us take the local maximum around $\mathfrak{f} \approx 1/10$ as the boundary shielding the finite-size effects. Still, the fit power for this fraction of the lattice does not meet Wolf's lower bound, while the determination coefficient R^2 has saturated to unity, so we cannot consider this portion of the lattice a thermodynamic regime.

Yet, it remains possible then that our system size is still too small for the thermodynamic limit to apply, and that larger systems may host thermodynamic regimes yet. Consider how the critical fraction $\mathfrak{f}_c$ defining the local maximum varies in size of the overall system. Figure 5.8 shows the critical fraction $\mathfrak{f}_c$ and critical order $\mathfrak{x}_c$ calculated over a family of lattices of varied size, and extrapolates back to the thermodynamic limit $1/L \to 0$ to probe for the thermodynamic fraction $\mathfrak{f}_T$ that the data suggest would saturate the fit-curve for an infinite system size. Notice that the critical fractions both trend upward with larger system sizes, and that the limit in the third-filled case is still larger than for the half-filled case. This suggests the finite-size parity effect on the entanglement scaling curve has finite extent, and that for a sufficiently large lattice, the trend may satisfy Wolf's bounds.

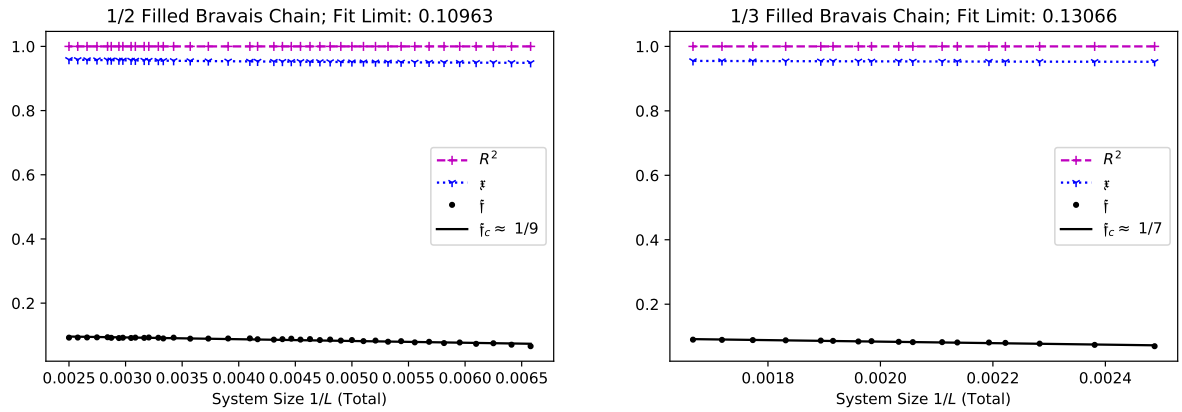

Figure 5.8: Calculating the critical fraction for a range of system sizes, a line is fit to the critical fraction $\mathfrak{f}_c$ and extrapolated back to probe the limits on the thermodynamic approximation $\ell \ll L$. The critical fraction is seen to increase with the size of the system, implying that the finite-size effects also have finite extent within the lattice.

Using the limit value of $\mathfrak{f} = 1/10$, a fit was performed on half-filled and third-filled lattices populated with up to 200 fermions. Figure 5.9 shows the resulting fit and the finite-size effect on the data points close to the centre of the lattice for the largest lattice. While both fit powers are just short of unity, our system is still far from infinite size, and we may be able to extrapolate to larger systems to check if there is a clear size for which the thermodynamic approximation may hold.

Performing the same fit with larger systems, we check whether this fraction $\mathfrak{f} = 1/10$ of the lattice will yield thermodynamic behaviour consistent with (5.1) for sufficiently large systems. Plotting the fit power $\mathfrak{x}$ against larger system sizes, in $1/L$, Figure 5.10, we see that there is an upward trend in the fit power for increasing system size. Taking a linear fit on the larger systems in the sample, to bound the trend from below, the data still fail to extrapolate back to values greater than unity, however, the upward curvature of the data obfuscate the meaning of this extrapolation. A quadratic fit fairs a little better on the data set, though still fails to reach unity. The range of the data here did not support convergent fits of either power-law or exponential form. Therefore, whether these data satisfy Wolf's

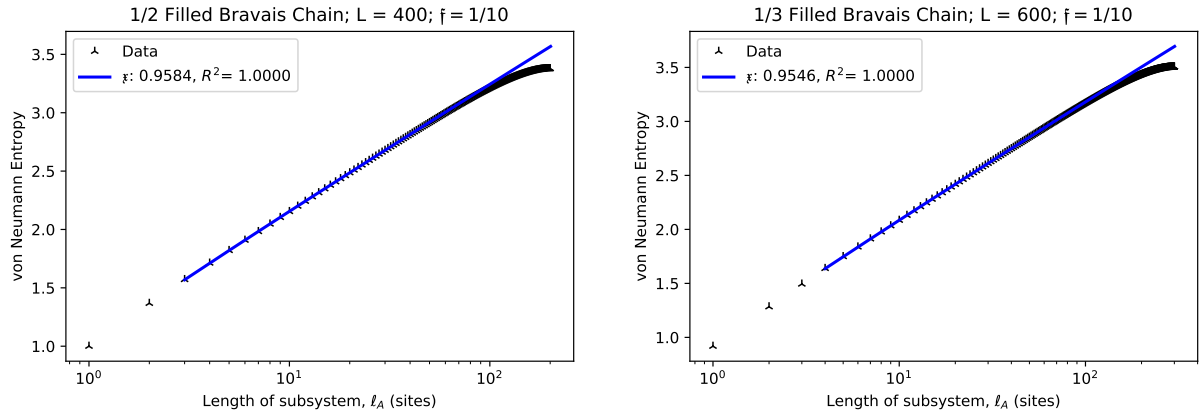

Figure 5.9: The von Neumann entropy scaling of a half-filled (left) and a third-filled (right) Bravais lattice with 200 fermions. Fitting a power law in $\log_2(\ell)$ over the first quarter of the chain, both fits fall just short of Wolf's lower bound.

bounds in the thermodynamic limit is unclear.

Thermodynamic Limit

An alternate approach to mitigate the parity effects of a finite system and better probe scaling in the thermodynamic limit, consider a family of ζ-filled lattices of varied populations $F = \zeta L$, fix a partitioning $\ell_A = \mathfrak{f} L$ for each lattice and investigate how these single-point entanglements change as we vary the length of the whole system. By taking the same point on the $S - vs - \ell_A$ curve for each lattice, the relative boundary effects are fixed, and we should be able to probe the thermodynamic limit more directly by fitting the aggregated data to a $\log^{\mathfrak{r}}(\ell)$ curve, as in Figure 5.11. Notice that the data on this curve still grow with the size of their respective lattice size, but no longer taper-off as we grow the subsystem. Then these data have transcended the scaling limitations enforced by the parity symmetry, such that the fitted curves satisfy Wolf's bounds consistently, although slight variation is seen for different lattice densities.

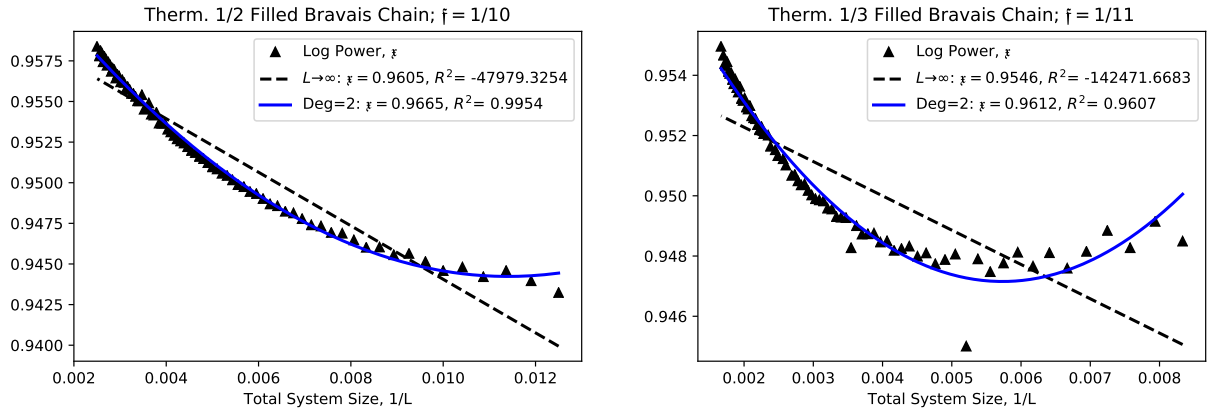

Figure 5.10: Extrapolating the logarithmic power using $\mathfrak{f} = 1/10$ of the uniform lattice chain toward the thermodynamic limit. Plotting the power against the inverse lattice length, we can probe the thermodynamic limit by extrapolating the data to $1/L = 0$.

Single-Body Correlators

To round out the analysis of the Bravais lattice, consider how the single-body correlation functions $C_{ij} = \langle c_i^\dagger c_j \rangle$ vary in the distance between sites i and j. Translational invariance in our model allows us to consider just the first row C_{0j} of the truncated correlation matrix, which is calculated for all partitions of the lattice. Figure 5.12 shows the decay profile of the rows in the correlation matrix from site $j = 0$ to site $j = \ell_A$ for the equal partitioning $\ell_A = L/2$. Quantum criticality of the Bravais lattice is confirmed as well, as we observe a power-law decay of these functions, implying long ranged correlations in the lattice.

Figure 5.12 also shows an oscillation in the correlations dependent on the filling of our lattice, as we find resonance for sites separated by integer multiples of the spatial density $\zeta^{-1}a$. These vanishing correlations are consequences of the Fermi statistics, which aims to maintain equal spacings between each of the fermions in the ground state in order to minimize the energy by maximizing possible hopping. Then, with an integer number of lattice sites per fermion ζ^{-1}, the single-body correlation function $\langle c_i^\dagger c_j \rangle$ vanishes for separations $|i - j|a = n\zeta^{-1}a$ for $n \in \mathbb{Z}$, as both sites i and j are either both vacant, or both occupied in the ground state, so that hopping between them is expected with zero probability.

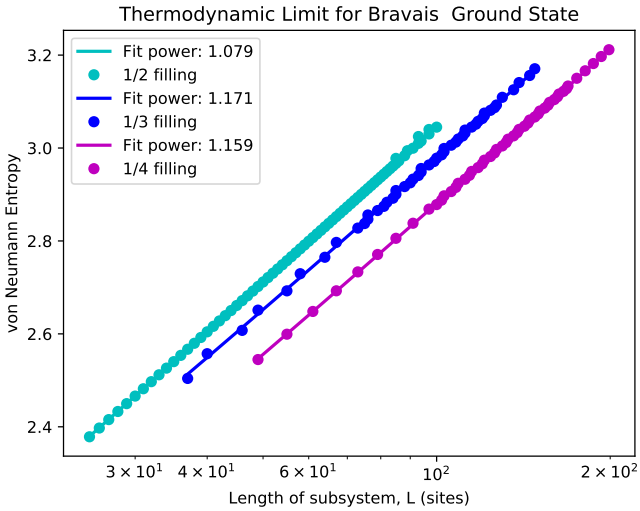

Figure 5.11: Fixing the filling $\zeta = 1/2,\ 1/3,\ 1/4$; and partition $\mathfrak{f} = 1/2$ we plot the entanglement scaling against the total system size and observe the logarithmic scaling as predicted by Wolf.

5.3.2 Gapped States - The SSH Model

Using the eigenstates of the SSH model, we again calculate the entanglement entropy at various bipartitions of fixed lattice systems to probe the scaling behaviour of a gapped system. From the dispersion relation, we see that our system is only gapped at half-filling, with the size of the gap $\Delta \sim 4|\delta|$ set by the dimerization δ of the lattice. For the half-filled lattice then, we expect the correlations between neighbouring sites to decay exponentially, and the entanglement entropy to saturate, as given by the area law in one dimension [24, 23]. These facts are verified below, and connected to the topological phase admitted by the model as well.

Correlation Length

The presence of a thermodynamic gap for the half-filled ground state of the SSH model localizes correlations such that the single-body correlator $C_{ij} = \langle c_i^\dagger c_j \rangle$ decays exponentially with the distance between two sites i and j, shown in Figure 5.13. As before, we see

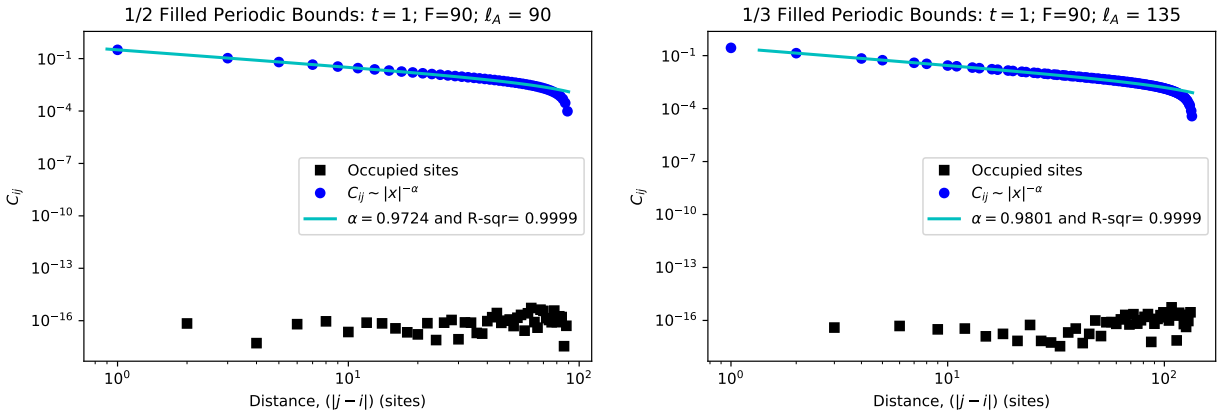

Figure 5.12: For the Bravais lattice, the single-body correlation function C_{ij} follows a power-law decay, indicative of a divergent correlation length. The splitting into two separate curves is a consequence of Fermi statistics, which ensures that each fermion in the ground state is even spaced from all others on the lattice. As a result, we see a value of zero for sites separated by distance $\zeta^{-1}a$.

an oscillation between this decay profile and vanishing correlation, caused by the Fermi statistics. The correlation length ξ is affected by the dimerization strength δ, such that more drastic dimerizations produce more localized correlations as expected, since greater dimerization suppresses the inter-cell coupling t_2. What is surprising is that the correlation length is consistently greater in the trivial phase ($\delta > 0$) than in the topological phase. This discrepancy between the two phases may arise from the type of mode we are correlating at the start of the chain. In the trivial phase, we see correlations for the paired mode on the first site, whereas the unpaired mode at the start of the topological chain is localized there by the weak coupling between itself and the next unit cell [108].

In the limit of full dimerization ($|\delta| \to 1$), the decay in the correlation becomes immediate, as inter-cell (intra-cell) hopping is suppressed by the vanishing coupling t_2 (t_1). We see this in Figure 5.14, where the correlation function only takes non-trivial values up to the edge of its unit cell. Changing the sign of δ we see either a full- or half-unit cell on the starting edge of the lattice, consistent with the paired- or un-paired edge modes that distinguish the trivial and topological phases, respectively.

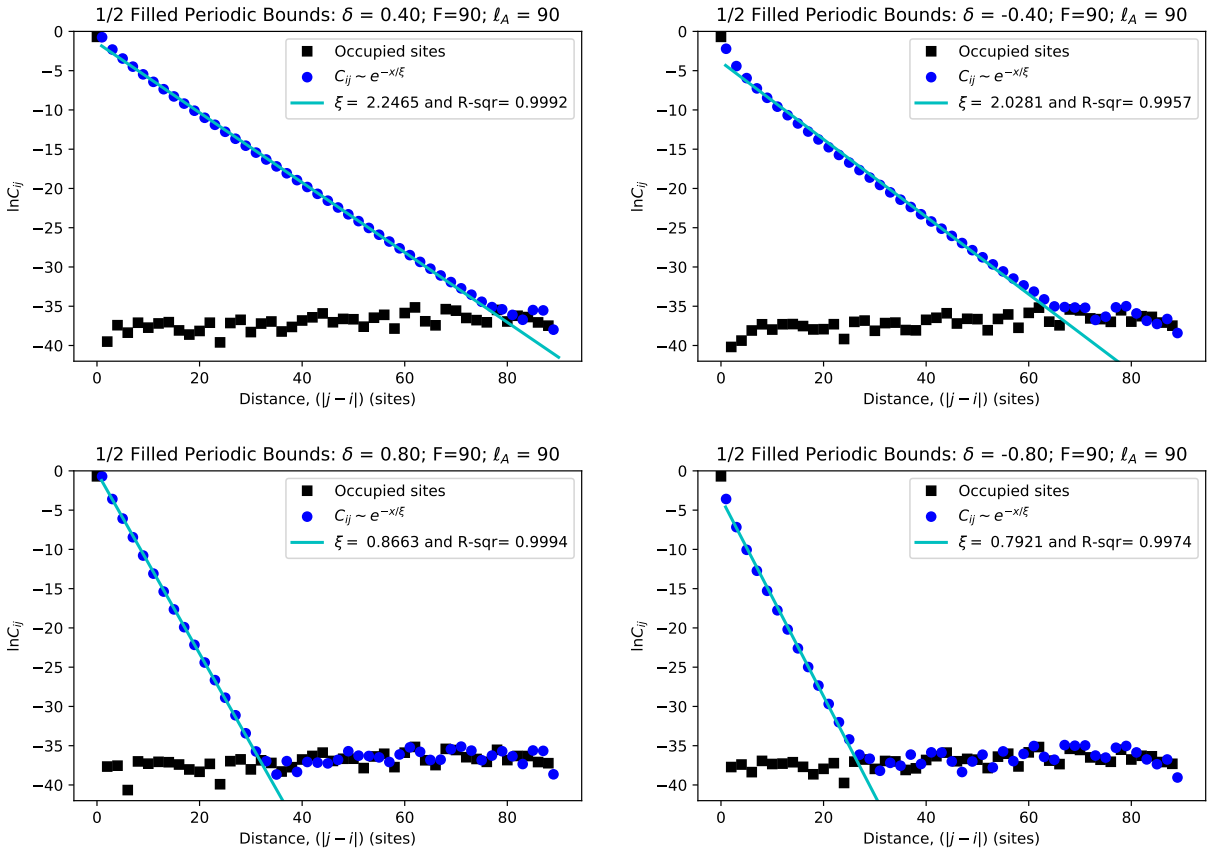

Figure 5.13: At half-filling, the single-body correlation function C_{ij} decays exponentially with finite correlation length ξ. The range of these correlations increase for weaker dimerizations (top) as well as in the trivial phase (left).

Oddly, the correlations of third-filled states under full dimerization still decay according to power laws (Figure 5.15), suggesting long ranged correlations persist within this insulating state. These correlations are likely an artefact of the degeneracy of the ground state, and indicative of a breaking-point in the Bloch wave model, since our model assumed waves spanning the entire lattice, for any dimerization δ. That two product wells should be correlated with one another appears to be a failing of the state function, under fallacious assumptions in this case. That the results survived as expected physically in the half-filled case is actually something of an enigma for the same reasons. These (fully dimerized) results should therefore be taken with a grain of salt, as they may reflect the limit cases of the model sooner

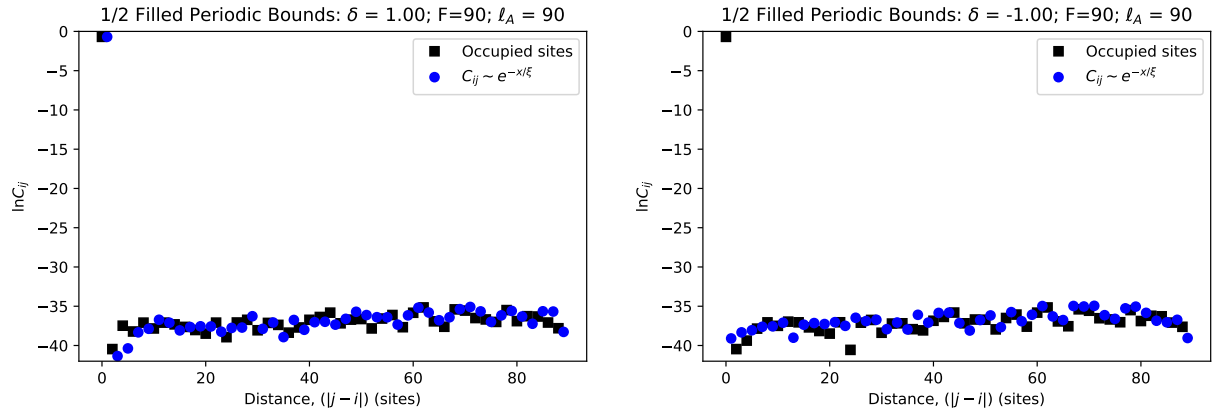

Figure 5.14: In the fully dimerized cases ($|\delta| = 1$), hopping between unit cells is forbidden since $t_i = 0$. We then see the single-body correlator vanish for any two sites in separate cells.

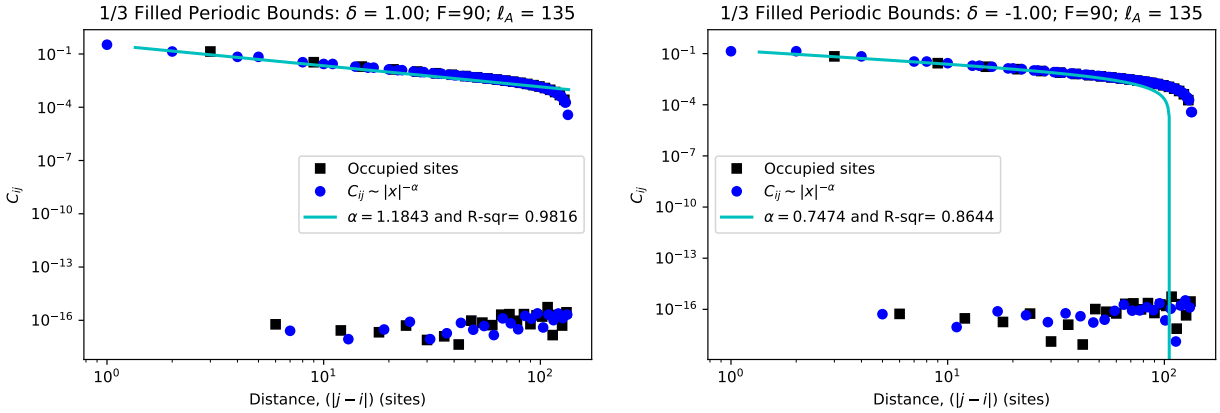

Figure 5.15: For third-filled states on the fully dimerized lattice ($|\delta| = 1$), correlations appear to still exist between unit cells even though hopping between them is strictly forbidden.

than fully physical phenomena.

For gapless states of the model, we see the correlations follow a power-law decay, similar to the states on the Bravais lattice. Figure 5.16 shows the form of the single-body correlator for a half-filled state at the critical point $\delta = 0$, and a third-filled state in the trivial phase. Both exhibit a power-law decay of their correlations, indicating long ranged correlations in the states. These results support the idea that it is the gapped-ness of the *state* that dictates its correlation behaviour, rather than the gapped-ness, or gapless-ness of the lattice itself, as both the gapped and gapless lattice can see power-law scaling.

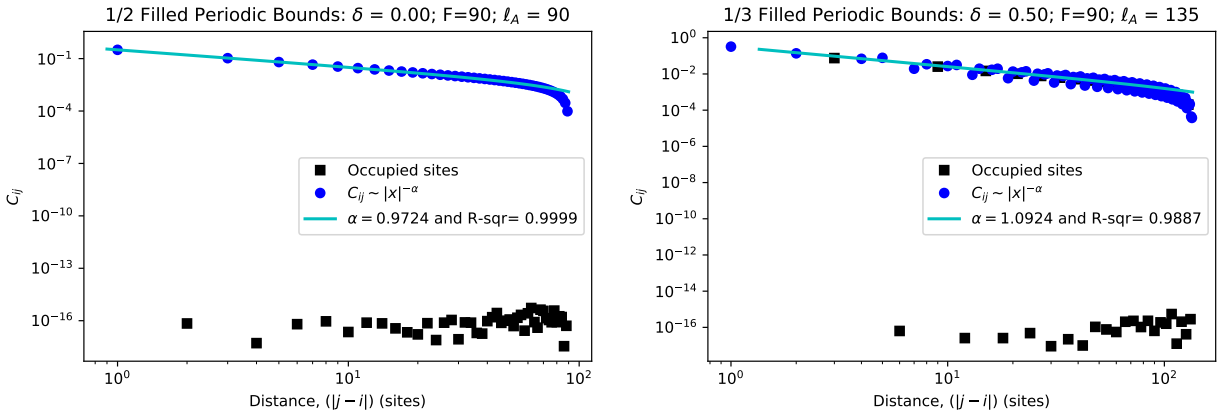

Figure 5.16: Gapless states at the critical point (left) and away from half-filling (right) both see a power-law in their correlations, as seen for the gapless states on the Bravais lattice.

5.3.3 Entanglement Scaling

The exponential decay of the single-body correlations within the gapped states of the SSH model is expected to prompt an asymptotic saturation in their entanglement entropy in one-dimension. For a half-filled state on a dimerized lattice, with $|\delta| \neq 0$, Figure 5.17 shows the entanglement trend split into two curves dependent on the parity of the subsystem. This stems from the alternating coupling strengths within the model (3.26), and whether the partition occurs within a unit cell, or between adjacent cells. For the topological case $\delta < 0$, and an even-length subsystem, the entanglement entropy counts strong correlation within two unit cells. Odd lengths on the other hand, only see entanglement within one cell, and between two others; even lengths in the trivial phase $\delta > 0$ measures only the entanglement between cells, and is the curve with consistently the least entropy. In each case, the entanglement saturates to an area law after just a few sites, with both the value and saturation depth determined by the strengths of the couplings across the partition boundary. This satisfies our intuition that the dimerization suppresses the range of correlations on the lattice, as we see a slight subsystem dependence only in the first few sites from an edge.

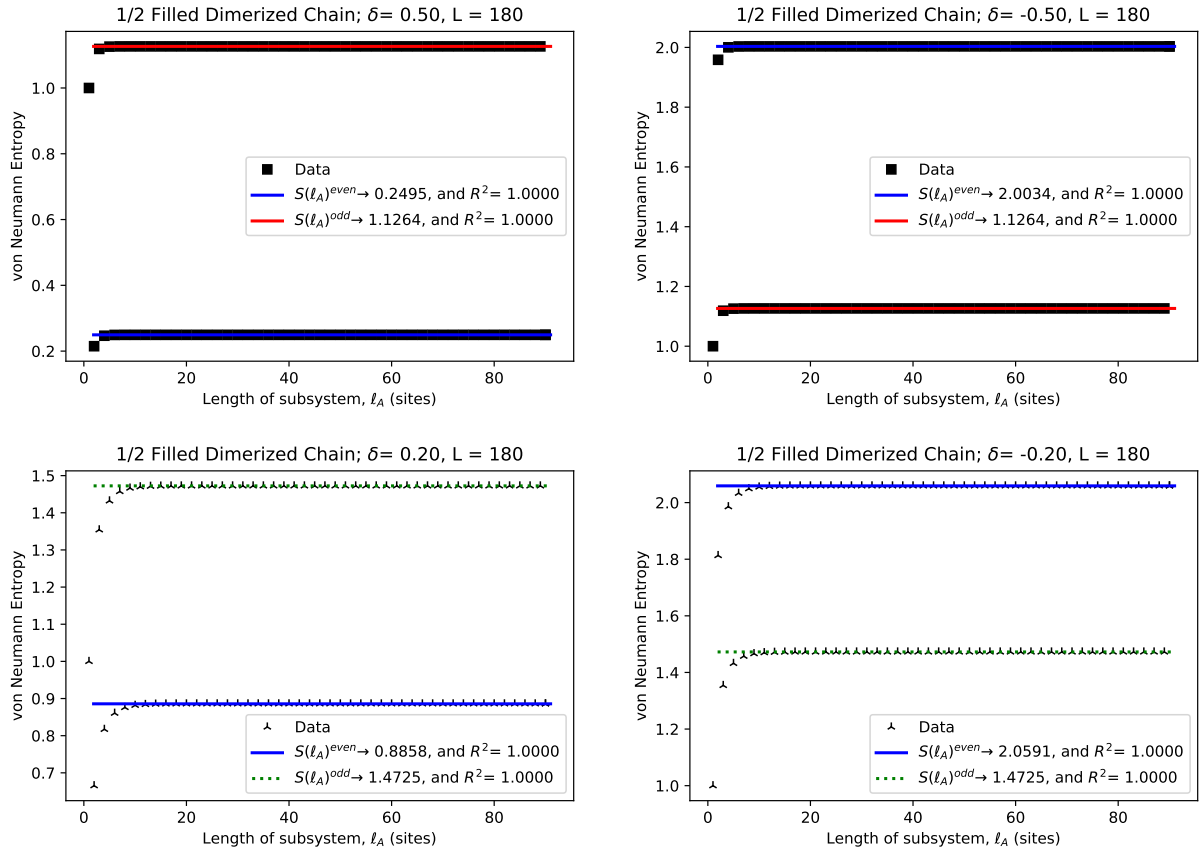

Figure 5.17: The von Neumann entropy scaling of a half-filled trivial (left, $\delta = 0.5,\ 0.2$) and topological (right, $\delta = -0.5,\ -0.2$) states of the SSH model with 90 fermions. For both, we see the entanglement saturate to clear area law scaling towards the middle of the chain, with the saturation expedited by greater dimerizations. Given periodic bounds, we see the difference in the number of edge modes counted by the entropy, as we partition within 0, 1,and 2 cells in the respective cases.

Limit Cases

Full dimerization yields a chain of product states with each two-site unit cells perfectly decoupled from the others. Since entanglement is identically zero for a product state, we can expect zero entanglement for a subsystem whose boundaries lie between unit cells. Figure 5.18 confirms this for both the trivial and topological phases, showing a perfect area-law of entanglement counting the number of unit cells split by our partition, equivalently counting the number of edge modes spanning the partition boundary.

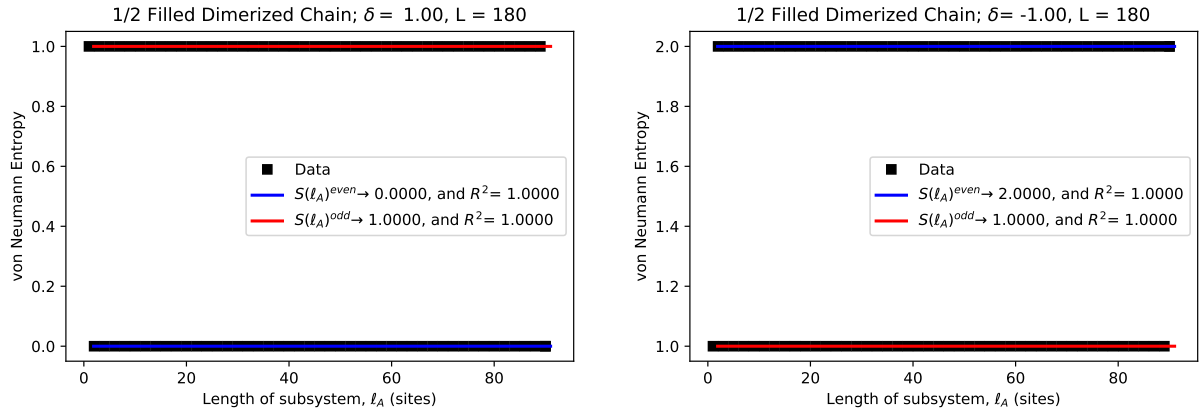

Figure 5.18: The von Neumann entropy scaling of a half-filled trivial ($\delta = 1$, left) and topological ($\delta = -1$, right) state of the SSH model with 90 fermions. We see area law scaling immediately in both. Given periodic bounds, we see the difference in the number of edge modes counted by the entropy, as we split 0, 1,and 2 cells with the respective partitions.

Conversely, as the dimerization decreases towards the critical point $\delta = 0$, the gap closes as the distinction between weak- and strong couplings vanishes and the lattice becomes uniform. In this limit, Figure 5.19 shows that the entanglement recovers the same scaling trend obtained for states on the Bravais lattice.

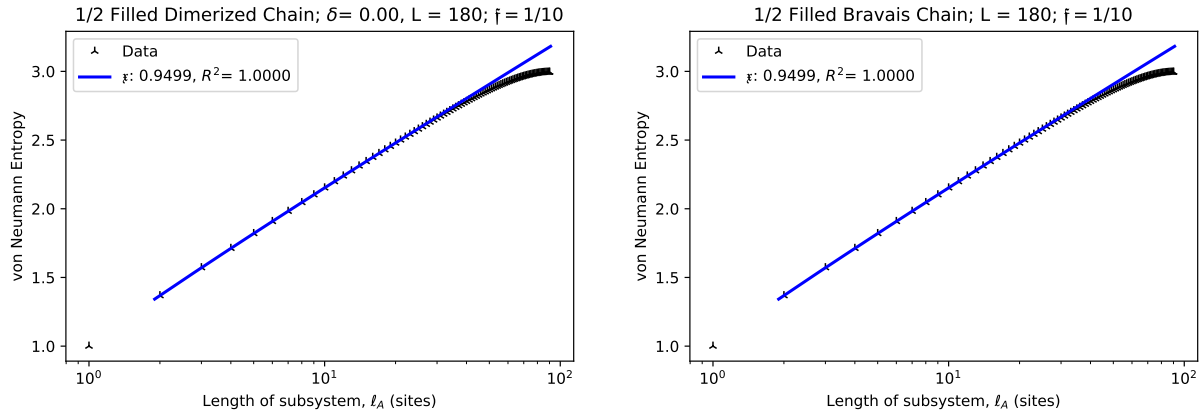

Figure 5.19: Setting $\delta = 0$ (left) we recover the logarithmic trends seen for the Bravais states (right), and verify that the entanglement witnesses the closing of the gap at this critical point.

5.3.4 Phase Transition

As we vary δ, we can study how the entanglement changes as our states change from the topological to the trivial phase of the model, and in particular, the behaviour around the critical point $\delta = 0$. Figure 5.20 shows the response of the entanglement at the centre of the lattice for half-filled states of 90 and 140 fermions as δ is varied between phases. We see that the entanglement peaks at the critical point, where it is known to violate the area law otherwise found in the adjacent gapped phases.

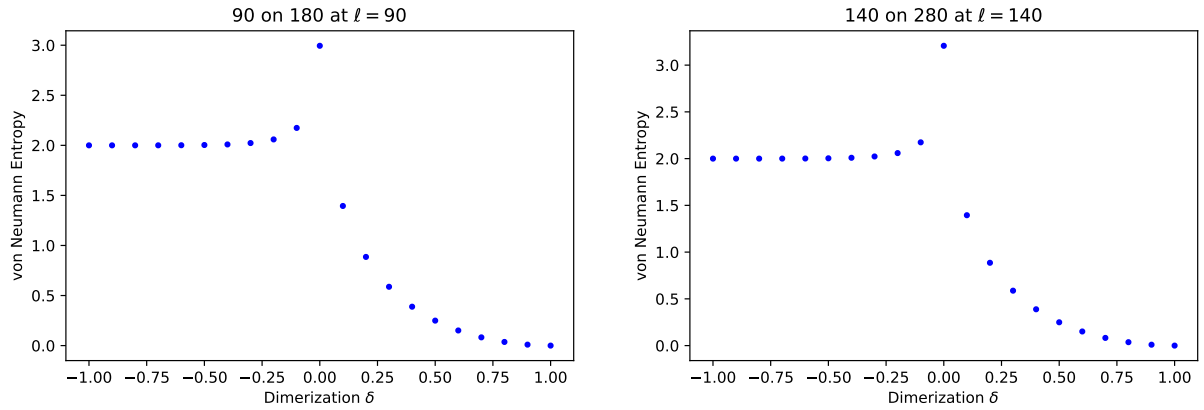

Figure 5.20: Plot of the von Neumann entropy at equal partition $\ell = L/2$ for a half-filled lattice of $F = 90,\ 140$ fermions at varying values of δ.

In the topological phase $\delta < 0$, the entanglement entropy measures the two edge modes of the even parity subsystem, compared to a single edge mode plus a weak-bond contribution in the trivial phase. Notice that in the topological phase, the entanglement is far less affected by (adiabatic) variations in δ than in the trivial phase. This is further evidence of the symmetry protected nature of the phase, as the contribution of the edge modes to the overall entanglement entropy is seen to be relatively flat outside of the vicinity of the phase boundary, where the symmetry defining the phase is broken [109]. For the trivial phase, on the other hand, we see entanglement contributions from the growing neighbourhoods of correlated modes, as the dimerization tends to zero. Notice as well, that the von Neumann

entropy demonstrates non-analytic behaviour at the critical point, in much the same way that other functions (such as the free energy) have identified (second-order) phase transitions traditionally. The entanglement entropy is therefore able to identify the topological phase transition in the SSH model, not only by the closing of the gap, but also by measuring the topological invariant (the number of edge modes) in the topological phase itself. The connection between entanglement and topological phases of matter is thus apparent in this system, and worth further investigation more broadly as well.

Chapter 6

Conclusions and Outlook

In this thesis, we have surveyed common numerical techniques for the calculation of the entanglement entropy of non-interacting fermionic ground states in one dimension. Starting from the eigenstates of two tight binding Hamiltonians, we saw three algorithms that calculate the von Neumann (entropy of) entanglement for a given contiguous partition of a fixed lattice system. These algorithms were analyzed by way of their accuracy and efficiency for these ground states and used to study the use of entanglement as a characterizer of quantum phase for two cases of fermionic quantum wires. In particular, the computation of entanglement entropy from the single-body correlation matrix is found to be the most efficient, by far, running in polynomial time with the size of the input system.

By calculating the vN entropy for many partitionings, we observed entanglement scaling trends for finite lattice systems that agree with previous analytical results in the thermodynamic limit [23, 24, 25]. Furthermore, these trends are shown to distinguish between a thermodynamically gapped and a gapless state, even in the finite lattice case.

In the case of a gapless state, the entanglement is seen to depend on the length of the smaller subsystem logarithmically, in violation of the area law. This logarithmic scaling derives from the long-ranged correlations within the state, which decay algebraically over

the length of the lattice. For systems of finite length, this logarithmic correction takes on sub-unit order, a result of finite-size effects represented by the parity symmetry within these systems. The order of the logarithmic fit is seen to increase with the size of the system, however, does not fall within the bounds put forth by Wolf [25] for any of the finite systems studied here, although it is not far short. Aggregating a family of finite-sized systems into a thermodynamic trend, the finite-size effects may be suppressed, so that the entanglement is found to satisfy Wolf's bounds.

For the gapped states of the SSH model, the entanglement entropy is seen to saturate to a constant value as described by an area law in 1D, even in finite systems. Intuitively, these localized correlations at the subsystem boundary is explained by the rapid decay of correlations within the gapped model. Further, the entanglement is able to see evidence of SPT modes on the un-paired edges of the SSH chain when we partition across a strong-coupling in the lattice. The invariance in the entanglement with changes to the dimerization away from the phase boundary witness the symmetry protected nature of this phase, counting the number of edge modes in the reduced system as the topological invariant of the phase. Further, the topological phase transition is evidenced by the entropy as it spikes at the critical point, where the band gap closes as the dimerization of the lattice vanishes. Moreover, that the form of this trend bears striking resemblance to the non-analytic points marking phase transitions traditionally supports the use of entanglement measures for the characterization of quantum phases, especially of the topological variety.

6.1 Outlook

The next step for this work is to investigate the entanglement spectrum in the trivial and topological phases, to study how information encoded within can further characterize these exotic phases. For topological phases especially, systems of two- and greater dimensions are

a natural extension, as greater dimensionality naturally fosters richer topology. Additionally, the extension of these methods to systems in higher dimensions is a great way to build physical intuition for area law behaviours more generally, which may assist the development of rigorous theories similar to those used in this work [24, 23]. It is these generalized area laws that perhaps are needed in order to fully connect with the striking parallels found in gravitational systems [75, 76, 77, 78, 79, 80], and formulate to a broader theory of informational quantum nature overall.

In terms of material science, many of the quantum phases of interest to forthcoming technologies exist in systems beyond the description of the tight binding model. To study the role of entanglement in any of these phases then requires the extension of our models to include terms for physical processes such as interactions and spin-orbit coupling, for example. The richer set of phases accessible from these extended models will provide some facets of the larger "material information theory" describing a broader range of experimental phenomena, especially relevant to pursuits in QIP. With these extended models, the advantage of exact diagonalization is lost, necessitating the use of other numerical techniques, such as the density matrix renormalization group (DMRG) [121, 122], in order to obtain the ground states of these models. From these extended systems as well, it will be imperative to identify efficient means to accurately obtain their entanglement spectra, should the methods surveyed in this work not suffice.

Bibliography

[1] S. Sachdev, "Quantum phase transitions," *Handbook of Magnetism and Advanced Magnetic Materials*, 2007.

[2] B. Zeng, *Quantum information meets quantum matter: From quantum entanglement to topological phases of many-body systems*. Springer, 2015.

[3] A. Schmitt, "Introduction to superfluidity," *Lect. Notes Phys*, vol. 888, no. 1, 2015.

[4] L. Savary and L. Balents, "Quantum spin liquids: A review," *Reports on Progress in Physics*, vol. 80, no. 1, p. 016502, 2016.

[5] X.-L. Qi and S.-C. Zhang, "Topological insulators and superconductors," *Reviews of Modern Physics*, vol. 83, no. 4, p. 1057, 2011.

[6] H. Nishimori and G. Ortiz, *Elements of phase transitions and critical phenomena*. Oxford: Oxford University Press, 2010.

[7] P. Hohenberg and A. Krekhov, "An introduction to the Ginzburg–Landau theory of phase transitions and nonequilibrium patterns," *Physics Reports*, vol. 572, pp. 1–42, 2015.

[8] L. Landau, "The theory of phase transitions," *Nature*, vol. 138, no. 3498, pp. 840–841, 1936.

[9] V. L. Ginzburg and L. D. Landau, "On the theory of superconductivity," in *On Superconductivity and Superfluidity*, pp. 113–137, Springer, 2009.

[10] X.-G. Wen, "Vacuum degeneracy of chiral spin states in compactified space," *Physical Review B*, vol. 40, no. 10, p. 7387, 1989.

[11] X.-G. Wen, "Topological orders in rigid states," *International Journal of Modern Physics B*, vol. 4, no. 02, pp. 239–271, 1990.

[12] A. Y. Kitaev, "Fault-tolerant quantum computation by anyons," *Annals of Physics*, vol. 303, no. 1, pp. 2–30, 2003.

[13] C. Nayak, S. H. Simon, A. Stern, M. Freedman, and S. D. Sarma, "Non-Abelian anyons and topological quantum computation," *Reviews of Modern Physics*, vol. 80, no. 3, p. 1083, 2008.

[14] D. J. Thouless, F. D. M. Haldane, and J. M. Kosterlitz, "The Nobel prize in physics 2016," *CURRENT SCIENCE*, vol. 111, no. 8, p. 1293, 2016.

[15] F. D. M. Haldane, "Nobel lecture: Topological quantum matter," *Reviews of Modern Physics*, vol. 89, no. 4, p. 040502, 2017.

[16] J. M. Kosterlitz, "Nobel lecture: Topological defects and phase transitions," *Reviews of Modern Physics*, vol. 89, no. 4, p. 040501, 2017.

[17] A. Osterloh, L. Amico, G. Falci, and R. Fazio, "Scaling of entanglement close to a quantum phase transition," *Nature*, vol. 416, no. 6881, p. 608, 2002.

[18] J. Eisert, M. Cramer, and M. B. Plenio, "Colloquium: Area laws for the entanglement entropy," *Reviews of Modern Physics*, vol. 82, no. 1, p. 277, 2010.

[19] A. Einstein, B. Podolsky, and N. Rosen, "Can quantum-mechanical description of physical reality be considered complete?," *Physical Review*, vol. 47, no. 10, p. 777, 1935.

[20] J. S. Bell, "On the Einstein Podolsky Rosen paradox," *Physics Physique Fizika*, vol. 1, no. 3, p. 195, 1964.

[21] R. Horodecki, P. Horodecki, M. Horodecki, and K. Horodecki, "Quantum entanglement," *Reviews of Modern Physics*, vol. 81, no. 2, p. 865, 2009.

[22] L. Carr, *Understanding quantum phase transitions*. CRC press, 2010.

[23] F. G. Brandão and M. Horodecki, "Exponential decay of correlations implies area law," *Communications in Mathematical Physics*, vol. 333, no. 2, pp. 761–798, 2015.

[24] M. B. Hastings, "An area law for one-dimensional quantum systems," *Journal of Statistical Mechanics: Theory and Experiment*, vol. 2007, no. 08, p. P08024, 2007.

[25] M. M. Wolf, "Violation of the entropic area law for fermions," *Physical Review Letters*, vol. 96, no. 1, p. 010404, 2006.

[26] F. G. Brandão, "Entanglement and quantum order parameters," *New Journal of Physics*, vol. 7, no. 1, p. 254, 2005.

[27] D. Cavalcanti, F. G. Brandão, and M. T. Cunha, "Entanglement quantifiers, entanglement crossover and phase transitions," *New Journal of Physics*, vol. 8, no. 10, p. 260, 2006.

[28] S.-J. Gu, S.-S. Deng, Y.-Q. Li, and H.-Q. Lin, "Entanglement and quantum phase transition in the extended Hubbard model," *Physical Review Letters*, vol. 93, no. 8, p. 086402, 2004.

[29] L. Lepori, G. De Chiara, and A. Sanpera, "Scaling of the entanglement spectrum near quantum phase transitions," *Physical Review B*, vol. 87, no. 23, p. 235107, 2013.

[30] Y. Ling, P. Liu, C. Niu, J.-P. Wu, and Z.-Y. Xian, "Holographic entanglement entropy close to quantum phase transitions," *Journal of High Energy Physics*, vol. 2016, no. 4, p. 114, 2016.

[31] A. Kitaev and J. Preskill, "Topological entanglement entropy," *Physical Review Letters*, vol. 96, no. 11, p. 110404, 2006.

[32] M. Levin and X.-G. Wen, "Detecting topological order in a ground state wave function," *Physical Review Letters*, vol. 96, no. 11, p. 110405, 2006.

[33] I. Bloch, "Ultracold quantum gases in optical lattices," *Nature Physics*, vol. 1, no. 1, p. 23, 2005.

[34] G. Jotzu, M. Messer, R. Desbuquois, M. Lebrat, T. Uehlinger, D. Greif, and T. Esslinger, "Experimental realization of the topological Haldane model with ultracold fermions," *Nature*, vol. 515, no. 7526, p. 237, 2014.

[35] M. A. Nielsen and I. L. Chuang, "Quantum information and quantum computation," *Cambridge: Cambridge University Press*, vol. 2, no. 8, p. 23, 2000.

[36] R. P. Feynman, "Simulating physics with computers," *International Journal of Theoretical Physics*, vol. 21, no. 6, pp. 467–488, 1982.

[37] J. I. Cirac, P. Zoller, H. J. Kimble, and H. Mabuchi, "Quantum state transfer and entanglement distribution among distant nodes in a quantum network," *Physical Review Letters*, vol. 78, no. 16, p. 3221, 1997.

[38] C.-W. Chou, J. Laurat, H. Deng, K. S. Choi, H. De Riedmatten, D. Felinto, and H. J. Kimble, "Functional quantum nodes for entanglement distribution over scalable quantum networks," *Science*, vol. 316, no. 5829, pp. 1316–1320, 2007.

[39] H. J. Kimble, "The quantum internet," *Nature*, vol. 453, no. 7198, p. 1023, 2008.

[40] R. Islam, R. Ma, P. M. Preiss, M. E. Tai, A. Lukin, M. Rispoli, and M. Greiner, "Measuring entanglement entropy in a quantum many-body system," *Nature*, vol. 528, no. 7580, p. 77, 2015.

[41] R. F. Werner, "Quantum states with Einstein-Podolsky-Rosen correlations admitting a hidden-variable model," *Physical Review A*, vol. 40, no. 8, p. 4277, 1989.

[42] C. H. Bennett and D. P. DiVincenzo, "Quantum information and computation," *Nature*, vol. 404, no. 6775, p. 247, 2000.

[43] W. K. Wootters, "Quantum entanglement as a quantifiable resource," *Philosophical Transactions of the Royal Society of London. Series A: Mathematical, Physical and Engineering Sciences*, vol. 356, no. 1743, pp. 1717–1731, 1998.

[44] H. J. Briegel, D. E. Browne, W. Dür, R. Raussendorf, and M. Van den Nest, "Measurement-based quantum computation," *Nature Physics*, vol. 5, no. 1, p. 19, 2009.

[45] R. Raussendorf, J. Harrington, and K. Goyal, "A fault-tolerant one-way quantum computer," *Annals of Physics*, vol. 321, no. 9, pp. 2242–2270, 2006.

[46] R. Raussendorf and H. J. Briegel, "A one-way quantum computer," *Physical Review Letters*, vol. 86, no. 22, p. 5188, 2001.

[47] R. Raussendorf, D. E. Browne, and H. J. Briegel, "Measurement-based quantum computation on cluster states," *Physical Review A*, vol. 68, no. 2, p. 022312, 2003.

[48] K. Inaba, Y. Tokunaga, K. Tamaki, K. Igeta, and M. Yamashita, "High-fidelity cluster state generation for ultracold atoms in an optical lattice," *Physical Review Letters*, vol. 112, no. 11, p. 110501, 2014.

[49] H. P. Nautrup and T.-C. Wei, "Symmetry-protected topologically ordered states for universal quantum computation," *Physical Review A*, vol. 92, no. 5, p. 052309, 2015.

[50] J.-C. Boileau, R. Laflamme, M. Laforest, and C. Myers, "Robust quantum communication using a polarization-entangled photon pair," *Physical Review Letters*, vol. 93, no. 22, p. 220501, 2004.

[51] D. Collins, N. Gisin, and H. De Riedmatten, "Quantum relays for long distance quantum cryptography," *Journal of Modern Optics*, vol. 52, no. 5, pp. 735–753, 2005.

[52] H. De Riedmatten, I. Marcikic, W. Tittel, H. Zbinden, D. Collins, and N. Gisin, "Long distance quantum teleportation in a quantum relay configuration," *Physical Review Letters*, vol. 92, no. 4, p. 047904, 2004.

[53] R. Valivarthi, Q. Zhou, G. H. Aguilar, V. B. Verma, F. Marsili, M. D. Shaw, S. W. Nam, D. Oblak, W. Tittel, *et al.*, "Quantum teleportation across a metropolitan fibre network," *Nature Photonics*, vol. 10, no. 10, p. 676, 2016.

[54] K. S. Choi, H. Deng, J. Laurat, and H. J. Kimble, "Mapping photonic entanglement into and out of a quantum memory," *Nature*, vol. 452, no. 7183, p. 67, 2008.

[55] E. Dennis, A. Kitaev, A. Landahl, and J. Preskill, "Topological quantum memory," *Journal of Mathematical Physics*, vol. 43, no. 9, pp. 4452–4505, 2002.

[56] A. I. Lvovsky, B. C. Sanders, and W. Tittel, "Optical quantum memory," *Nature Photonics*, vol. 3, no. 12, p. 706, 2009.

[57] G. Vidal, "Entanglement monotones," *Journal of Modern Optics*, vol. 47, no. 2-3, pp. 355–376, 2000.

[58] M. B. Plenio and S. S. Virmani, "An introduction to entanglement theory," in *Quantum Information and Coherence*, pp. 173–209, Springer, 2014.

[59] N. Laflorencie, "Quantum entanglement in condensed matter systems," *Physics Reports*, vol. 646, pp. 1–59, 2016.

[60] N. Regnault, *Entanglement spectroscopy and its application to the fractional quantum Hall phases*. PhD thesis, Ecole Normale Supérieure de Paris-ENS Paris, 2013.

[61] V. Vedral and M. B. Plenio, "Entanglement measures and purification procedures," *Physical Review A*, vol. 57, no. 3, p. 1619, 1998.

[62] D. Petz, "Entropy, von Neumann and the von Neumann entropy," in *John von Neumann and the Foundations of Quantum Physics*, pp. 83–96, Springer, 2001.

[63] I. Bengtsson and K. Życzkowski, *Geometry of quantum states: An introduction to quantum entanglement*. Cambridge university press, 2017.

[64] A. Rényi *et al.*, "On measures of entropy and information," in *Proceedings of the Fourth Berkeley Symposium on Mathematical Statistics and Probability, Volume 1: Contributions to the Theory of Statistics*, The Regents of the University of California, 1961.

[65] M. Müller-Lennert, F. Dupuis, O. Szehr, S. Fehr, and M. Tomamichel, "On quantum Rényi entropies: A new generalization and some properties," *Journal of Mathematical Physics*, vol. 54, no. 12, p. 122203, 2013.

[66] J. C. Baez, "Rényi entropy and free energy," *arXiv preprint arXiv:1102.2098*, 2011.

[67] P. Jizba and T. Arimitsu, "The world according to Renyi: Thermodynamics of fractal systems," in *AIP Conference Proceedings*, vol. 597, pp. 341–348, AIP, 2001.

[68] X. Dong, "The gravity dual of Rényi entropy," *Nature Communications*, vol. 7, p. 12472, 2016.

[69] M. Berta, K. P. Seshadreesan, and M. M. Wilde, "Rényi generalizations of the conditional quantum mutual information," *Journal of Mathematical Physics*, vol. 56, no. 2, p. 022205, 2015.

[70] P. Hayden and A. Winter, "Communication cost of entanglement transformations," *Physical Review A*, vol. 67, no. 1, p. 012326, 2003.

[71] J. San Kim and B. C. Sanders, "Monogamy of multi-qubit entanglement using Rényi entropy," *Journal of Physics A: Mathematical and Theoretical*, vol. 43, no. 44, p. 445305, 2010.

[72] J. D. Bekenstein, "Statistical black-hole thermodynamics," *Physical Review D*, vol. 12, no. 10, p. 3077, 1975.

[73] J. D. Bekenstein, "Bekenstein-Hawking entropy," *Scholarpedia*, vol. 3, no. 10, p. 7375, 2008.

[74] S. W. Hawking, "Black holes and thermodynamics," *Physical Review D*, vol. 13, no. 2, p. 191, 1976.

[75] L. McGough and H. Verlinde, "Bekenstein-Hawking entropy as topological entanglement entropy," *Journal of High Energy Physics*, vol. 2013, no. 11, p. 208, 2013.

[76] S. Sachdev, "Bekenstein-Hawking entropy and strange metals," *Physical Review X*, vol. 5, no. 4, p. 041025, 2015.

[77] A. Strominger and C. Vafa, "Microscopic origin of the Bekenstein-Hawking entropy," *Physics Letters B*, vol. 379, no. 1-4, pp. 99–104, 1996.

[78] S. Ryu and Y. Hatsugai, "Entanglement entropy and the Berry phase in the solid state," *Physical Review B*, vol. 73, no. 24, p. 245115, 2006.

[79] B. Swingle, "Spacetime from entanglement," *Annual Review of Condensed Matter Physics*, vol. 9, pp. 345–358, 2018.

[80] M. Van Raamsdonk, "Building up spacetime with quantum entanglement," *General Relativity and Gravitation*, vol. 42, no. 10, pp. 2323–2329, 2010.

[81] C. Herdman, P.-N. Roy, R. Melko, and A. Del Maestro, "Entanglement area law in superfluid 4 He," *Nature Physics*, vol. 13, no. 6, p. 556, 2017.

[82] F. G. Brandão and M. Cramer, "Entanglement area law from specific heat capacity," *Physical Review B*, vol. 92, no. 11, p. 115134, 2015.

[83] I. Frérot and T. Roscilde, "Area law and its violation: A microscopic inspection into the structure of entanglement and fluctuations," *Physical Review B*, vol. 92, no. 11, p. 115129, 2015.

[84] B. Swingle and J. McGreevy, "Area law for gapless states from local entanglement thermodynamics," *Physical Review B*, vol. 93, no. 20, p. 205120, 2016.

[85] J. D. Patterson and B. C. Bailey, *Solid-state physics: Introduction to the theory*. Springer Science & Business Media, 2007.

[86] M. Greiner, O. Mandel, T. Esslinger, T. W. Hänsch, and I. Bloch, "Quantum phase transition from a superfluid to a Mott insulator in a gas of ultracold atoms," *Nature*, vol. 415, no. 6867, p. 39, 2002.

[87] K. Yang, K. Moon, L. Zheng, A. MacDonald, S. Girvin, D. Yoshioka, and S.-C. Zhang, "Quantum ferromagnetism and phase transitions in double-layer quantum Hall systems," *Physical Review Letters*, vol. 72, no. 5, p. 732, 1994.

[88] P. Bak, *How nature works: The science of self-organized criticality*. Springer Science & Business Media, 2013.

[89] H. Li and F. D. M. Haldane, "Entanglement spectrum as a generalization of entanglement entropy: Identification of topological order in non-Abelian fractional quantum Hall effect states," *Physical Review Letters*, vol. 101, no. 1, p. 010504, 2008.

[90] H.-C. Jiang, Z. Wang, and L. Balents, "Identifying topological order by entanglement entropy," *Nature Physics*, vol. 8, no. 12, p. 902, 2012.

[91] F. Pollmann, A. M. Turner, E. Berg, and M. Oshikawa, "Entanglement spectrum of a topological phase in one dimension," *Physical Review B*, vol. 81, no. 6, p. 064439, 2010.

[92] P. A. Martin and F. Rothen, *Many-body problems and quantum field theory: An introduction*, pp. 90–92. Springer Science & Business Media, 2013.

[93] C. P. Burgess, "Goldstone and pseudo-Goldstone bosons in nuclear, particle and condensed-matter physics," *Physics Reports*, vol. 330, no. 4, pp. 193–261, 2000.

[94] T. Brauner, "Spontaneous symmetry breaking and Nambu–Goldstone bosons in quantum many-body systems," *Symmetry*, vol. 2, no. 2, pp. 609–657, 2010.

[95] T. Kita, "Properties of Nambu–Goldstone bosons in a single-component Bose–Einstein condensate," *Journal of the Physical Society of Japan*, vol. 80, no. 8, p. 084606, 2011.

[96] G. Volovik and M. Zubkov, "Higgs bosons in particle physics and in condensed matter," *Journal of Low Temperature Physics*, vol. 175, no. 1-2, pp. 486–497, 2014.

[97] M. De Llano, F. Sevilla, and S. Tapia, "Cooper pairs as bosons," *International Journal of Modern Physics B*, vol. 20, no. 20, pp. 2931–2939, 2006.

[98] M. Cramer, J. Eisert, M. B. Plenio, and J. Dreißig, "Entanglement-area law for general bosonic harmonic lattice systems," *Physical Review A*, vol. 73, no. 1, p. 012309, 2006.

[99] S. B. Bravyi and A. Y. Kitaev, "Fermionic quantum computation," *Annals of Physics*, vol. 298, no. 1, pp. 210–226, 2002.

[100] D. L. Feder, "Maximally entangled gapped ground state of lattice fermions," *Physical Review A*, vol. 85, no. 1, p. 012312, 2012.

[101] C. Xin and S. Yun, "Fermionic one-way quantum computation," *Chinese Physics Letters*, vol. 31, no. 11, p. 110302, 2014.

[102] A. Tranter, S. Sofia, J. Seeley, M. Kaicher, J. McClean, R. Babbush, P. V. Coveney, F. Mintert, F. Wilhelm, and P. J. Love, "The Bravyi–Kitaev transformation: Properties and applications," *International Journal of Quantum Chemistry*, vol. 115, no. 19, pp. 1431–1441, 2015.

[103] J. T. Seeley, M. J. Richard, and P. J. Love, "The Bravyi-Kitaev transformation for quantum computation of electronic structure," *The Journal of Chemical Physics*, vol. 137, no. 22, p. 224109, 2012.

[104] B. M. Terhal and D. P. DiVincenzo, "Classical simulation of noninteracting-fermion quantum circuits," *Physical Review A*, vol. 65, no. 3, p. 032325, 2002.

[105] D. J. Brod and E. F. Galvao, "Extending matchgates into universal quantum computation," *Physical Review A*, vol. 84, no. 2, p. 022310, 2011.

[106] N. Ashcroft and N. Mermin, *Solid State Physics*. Philadelphia: Saunders College, 1976.

[107] W. Su, J. Schrieffer, and A. J. Heeger, "Solitons in polyacetylene," *Physical Review Letters*, vol. 42, no. 25, p. 1698, 1979.

[108] J. Sirker, M. Maiti, N. Konstantinidis, and N. Sedlmayr, "Boundary fidelity and entanglement in the symmetry protected topological phase of the SSH model," *Journal of Statistical Mechanics: Theory and Experiment*, vol. 2014, no. 10, p. P10032, 2014.

[109] J. K. Asbóth, L. Oroszlány, and A. Pályi, "A short course on topological insulators," *Lecture Notes in Physics*, vol. 919, 2016.

[110] J. Cho and K. W. Kim, "Quantum phase transition and entanglement in topological quantum wires," *Scientific Reports*, vol. 7, no. 1, p. 2745, 2017.

[111] E. J. Meier, F. A. An, and B. Gadway, "Observation of the topological soliton state in the Su–Schrieffer–Heeger model," *Nature Communications*, vol. 7, p. 13986, 2016.

[112] G. Van Rossum and F. L. Drake, *Python reference manual*. iUniverse, 2000.

[113] T. E. Oliphant, *A guide to NumPy*, vol. 1. Trelgol Publishing USA, 2006.

[114] E. Anderson, Z. Bai, C. Bischof, S. Blackford, J. Dongarra, J. Du Croz, A. Greenbaum, S. Hammarling, A. McKenney, and D. Sorensen, *LAPACK Users' guide*, vol. 9. Siam, 1999.

[115] I. Peschel, "Calculation of reduced density matrices from correlation functions," *Journal of Physics A: Mathematical and General*, vol. 36, no. 14, p. L205, 2003.

[116] H. Li and F. D. M. Haldane, "Entanglement spectrum as a generalization of entanglement entropy: Identification of topological order in non-Abelian fractional quantum Hall effect states," *Physical Review Letters*, vol. 101, no. 1, p. 010504, 2008.

[117] I. Peschel and V. Eisler, "Reduced density matrices and entanglement entropy in free lattice models," *Journal of Physics A: Mathematical and Theoretical*, vol. 42, no. 50, p. 504003, 2009.

[118] I. Peschel and M.-C. Chung, "On the relation between entanglement and subsystem Hamiltonians," *EPL (Europhysics Letters)*, vol. 96, no. 5, p. 50006, 2011.

[119] J. Latorre and A. Riera, "A short review on entanglement in quantum spin systems," *Journal of Physics A: Mathematical and Theoretical*, vol. 42, no. 50, p. 504002, 2009.

[120] L. Vidmar, L. Hackl, E. Bianchi, and M. Rigol, "Entanglement entropy of eigenstates of quadratic fermionic Hamiltonians," *Physical Review Letters*, vol. 119, no. 2, p. 020601, 2017.

[121] U. Schollwöck, "The density-matrix renormalization group," *Reviews of Modern Physics*, vol. 77, no. 1, p. 259, 2005.

[122] S. R. White, "Density-matrix algorithms for quantum renormalization groups," *Physical Review B*, vol. 48, no. 14, p. 10345, 1993.